

# **Development of stage-scanning electron holography**

## **試料走査電子線ホログラフィー法の開発**

**埼玉工業大学大学院 工学研究科**

**電子工学専攻**

**Lei Dan**

**雷 丹**

## Contents

ABSTRACT.....	I
Chapter 1 Introduction of electron holography.....	1
1.1 Transmission electron microscopy.....	1
1.2 Overview and history of electron holography .....	2
1.3 Theoretical basis of off-axis electron holography.....	4
1.3.1 Hologram formation in off-axis electron holography.....	5
1.3.2 Hologram reconstruction .....	7
1.3.3 Phase shift by magnetic and electric fields .....	10
1.3.4 Applications of off-axis electron holography .....	12
1.4 Other Forms of electron holography.....	13
1.5 Other techniques for phase measurement .....	16
1.5.1 Phase measurement using the transport of intensity equation .....	16
1.5.2 Phase measurement using Lorentz microscopy .....	17
1.6 Aims and contents in this thesis .....	19
Reference .....	21
Chapter 2 Development of stage-scanning electron holography.....	25
2.1 Introduction.....	25
2.2 Development of stage-scanning electron holography.....	26
2.2.1 Principle and experimental methods.....	26
2.2.2 Results and discussion .....	29
2.3 Stage-scanning electron holography with a digital aperture.....	32
2.3.1 Methods.....	32
2.3.2 Results and disctssion .....	33
2.4 Conclusions.....	35
Reference .....	36
Chapter 3 Improvement of stage-scanning electron holography .....	38

3.1 Introduction.....	38
3.2 Improvement of stage-scanning electron holography for a non-phase object	39
3.2.1 Principle .....	39
3.2.2 Experimental methods .....	44
3.2.3 Results and discussion .....	44
3.2.4 Drift effect of the biprism and specimen stage and considerations for recording .....	50
3.3 Demonstration of resolution improvement in stage-scanning electron holography .....	54
3.3.1 Experimental methods .....	54
3.3.2 Results and discussion .....	56
3.4 Conclusions.....	58
Reference .....	60
Chapter 4 Super-resolution phase reconstruction technique in stage-scanning electron holography .....	62
4.1 Introduction.....	62
4.2 Principle .....	64
4.2.1 Scan step is a multiple of the CCD pixel size.....	65
4.2.2 Arbitrary scan step .....	67
4.3 Simulation for super resolution electron holography.....	69
4.4 Experimental methods .....	72
4.5 Results and discussion .....	73
4.6 Fresnel diffraction effect.....	75
4.7 Conclusions.....	77
Reference .....	78
Chapter 5 Conclusions .....	81
Acknowledgements.....	83
Publication List.....	85

## **ABSTRACT**

Electron holography is a powerful electron-interference technique through the use of transformation electron microscopes (TEMs). Contrary to the conventional TEM techniques, which record only the image intensity, electron holography yields both the phase and amplitude of the electron wave that passed through a specimen. The successful developments of field-emission electron guns and electron biprisms made electron holography a practical tool allowing quantitative and precise measurements. In recent research, off-axis electron holography is the most widely used holography technique. In this technique, Fourier transformation is commonly used for the phase-retrieval. However, the spatial resolution of the reconstructed phase image is limited by the fringe spacing of the hologram. Therefore, how to improve the spatial resolution of the reconstructed phase images becomes an important topic in electron holography field.

This thesis mainly concentrates on the development of a stage-scanning electron holography technique with a stage-scanning system, which overcomes the limitation between the spatial resolution and the fringe spacing of the hologram. Firstly, the stage-scanning electron holography technique under phase object approximation is presented. This technique is used to acquire an interferogram, that is, cosine image of phase distribution. The interferogram is constructed by shifting the specimen in one direction with a stage-scanning system and acquiring line intensities of holograms. Taking line intensities eliminates the carrier fringes in the holograms and yields the interferogram. Under phase object approximation, the object phase can be readily obtained from the interferogram without any reconstruction procedure. The spatial resolution of phase is determined independently of the fringe spacing, overcoming the limitation of conventional techniques based on the Fourier transformation method. Then this technique was improved for non-phase object with a reconstruction procedure. The resolution improvement was demonstrated by observing cobalt

nanoparticles using the stage-scanning holography and the conventional holography, and significantly sharper images were obtained with the former technique.

In the stage-scanning electron holography, the step size is a key parameter during the stage scan. If the scanning step is a multiple of the CCD pixel size then the spatial resolution of the reconstructed phase image is determined by the CCD pixel size divided by magnification, or the microscope resolution. If the scanning step is an arbitrary, in which the holograms are recorded with sub-pixel specimen shifts, therefore these holograms provide different phase information. In this case, super-resolution reconstruction technique is introduced into stage-scanning electron holography. The processing of the acquired series of holograms with sub-pixel specimen shifts result in a higher pixel density and spatial resolution as compared to the phase image obtained with conventional holography. The final resolution exceeds the limit of the CCD pixel size divided by the magnification.

**Keywords:** Electron holography, stage scanning, spatial resolution, phase shift, super resolution

## **Chapter 1 Introduction of electron holography**

### **1.1 Transmission electron microscopy**

Transmission electron microscopy (TEM) has revolutionized our understanding of materials and introduces us into nano-world by completing the processing-structure-properties links down to atomistic levels [1-15]. TEM is powerful tool which can provide almost all the structural, phase, and crystallographic data and allow us to observe nanometer sized object [1].

In TEM, an electron beam of electrons is transmitted through an ultra-thin specimen. The transmitted electron beam interacts with the specimen. From the interaction between the electron beam and the specimen, an image is formed; the image is then magnified and focused by the electron lens in the TEM column onto an imaging device, such as a fluorescent screen, on a layer of photographic film, or to be detected by a sensor such as a charge-coupled device (CCD) camera.

Ruska and Knoll built the first TEM in the early 1930s [2, 3]. In 1939, electron microscope became commercial. The first commercial electron microscope was installed in the Physics department of I. G Farben-Werke [4]. TEMs became widely available by several companies such as Hitachi, JEOL, Philips, etc since the late of 1940s.

A usual TEM instrument is constituted with three parts: the lens column, the vacuum system and the supplying and controlling system. The lens column is the most important and complicated part of a TEM, which mainly contains electron guns, illumination system, imaging system and the observation and recording system, as shown in Fig.1.1 [8]. The objective lens and the specimen stage system is the heart of the TEM. This critical region usually extends over a distance of ~10mm at the center

of the TEM. The imaging system contains some intermediate lenses which can magnify the image or the diffraction pattern produced by the objective lens and to focus them on the viewing screen or computer display via a detector, CCD or TV camera.

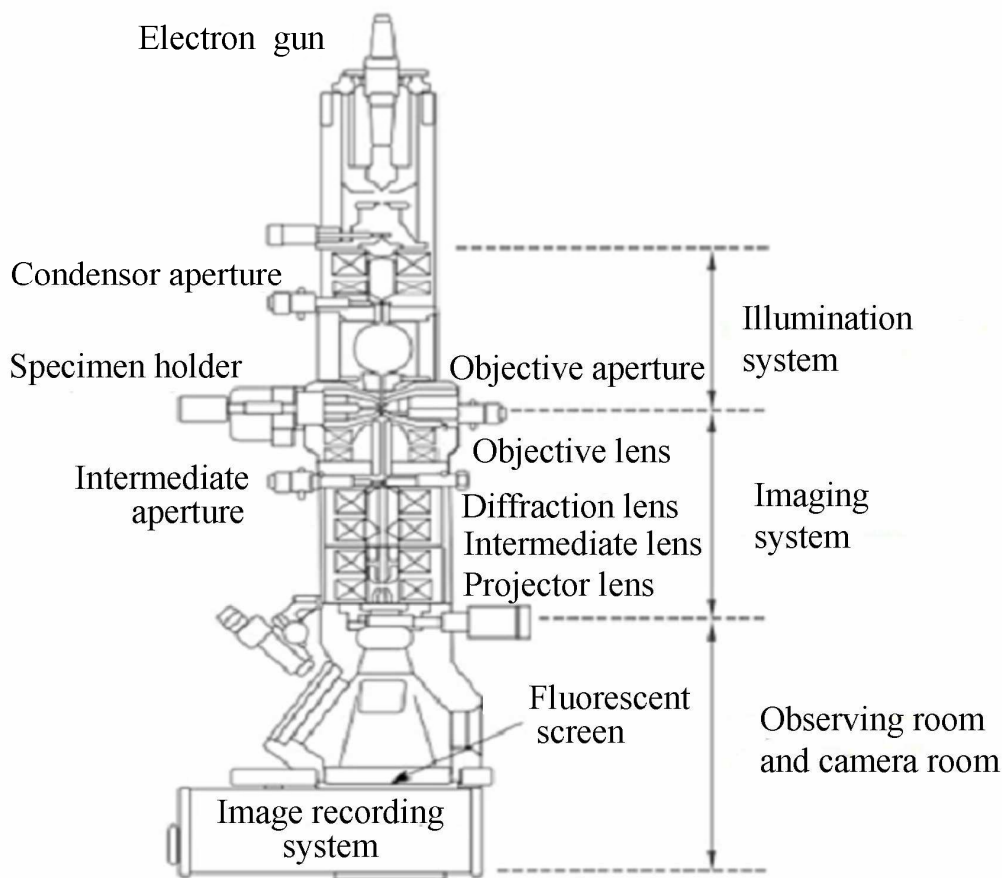


Fig. 1.1 Schematic of optical components in a basic TEM [8].

## 1.2 Overview and history of electron holography

Electron holography is a powerful electron-interference technique through the use of TEMs [16, 17]. The conventional TEM techniques only record the spatial distribution of image intensity in the final image, however, electron holography enables us to access both the amplitude and phase of the electron wave that has passed through a specimen. The phase distribution is important because most object

information is encoded in the phase of the transmitted electron wave. However, conventional TEM is blind to these object properties, for example, electric or magnetic fields in the specimen. Since the phase can only be detected by interferometric means, electron holography has paved the way for a comprehensive analysis of nearly all object properties at medium and atomic resolution.

D. Gabor [18] originally proposed the electron holography technique as a means of overcoming the spherical aberration of the TEM objective lens. A lens-less imaging method was developed from Gabor's idea [19]: the object wave propagates in space according to the well-known wave equation, if the complete wave with amplitude and phase can be recorded by means of a detector at some distance, the wave can be back-propagated according to the same wave equation. An important point is that the detector must record the propagated wave completely, that means both amplitude and phase should be recorded. Gabor made this point out by interfering the propagated wave with a known reference wave. The arising interference fringes are modulated in contrast and position by amplitude and phase of the wave, respectively. Then the wave can be recorded as an interference pattern, which is named as "hologram" by Gabor.

In 1951, Haine and Mulvey [20] recorded electron holograms firstly; they called the holograms as Fresnel in line holograms. They reached about 1 nm of the specimen details in the reconstructed wave. However, the resolution of the reconstructed wave was limited by the twin-image problem. That is because, in Gabor's in-line holography technique, the reference wave propagates in the same direction as the object wave. Under reconstruction, two conjugate waves (twin-waves) arise, which overlap coherently and hence cannot be separated from each other. However, this twin-image problem was solved by Leith and Upatnieks [21]. They proposed to superimpose reference and object wave at an angle  $\beta$ . Then the reconstructed twin-waves are separated angularly by  $2\beta$  from each other in Fourier space.

In light optics, the laser can be seen as a nearly perfectly coherent light source, thus, holography is widespread in various holographic techniques. The hologram may be recorded in the near-field (Fresnel holograms), in the far-field (Fraunhofer hologram),

in the Fourier-spectrum (Fourier hologram), etc [22].

In contrast to light holography using the laser, electron holography started flourishing much later, because it is much more difficult to satisfy the requirement of electron coherence. Therefore, coherent electron optics was performed only in a few especially experienced laboratories. For example, off-axis electron interferometry was developed and well understood by Möllenstedt and co-workers from 1954. In 1968, Möllenstedt and Wahl [23], recorded the first lens-less (no objective lens) off-axis Fresnel hologram and successfully reconstructed the electron wave with laser light. However, thinking about the limits of this method, Wahl recognized that lens-less imaging is not promising for electron holography, because the achievable resolution is limited by the restricted degree of spatial coherence of electrons. Therefore, from light optics Wahl adopted the method of image plane off-axis holography into electron microscopy and developed image plane off-axis electron holography [24]. To date, this is the most successful and widespread holographic method applied in electron microscopy.

### **1.3 Theoretical basis of off-axis electron holography**

Since the original proposal by Gabor for the use of holography as a means for the improvement of the resolution of electron microscopes, a number of schemes for electron holography have been proposed and several of these have been demonstrated experimentally. These include in-line holography, off-axis holography, and phase-shifting holography, etc [25]. However, in recent materials research using electron holography, off-axis electron holography attracts most attention in electron holography field. This particular holographic operating mode is advantageous in that it is easily obtained in any commercial TEM with field-emission gun (FEG) [26], and it is the mode that has been used almost exclusively in recent electron microscopy studies.

### 1.3.1 Hologram formation in off-axis electron holography

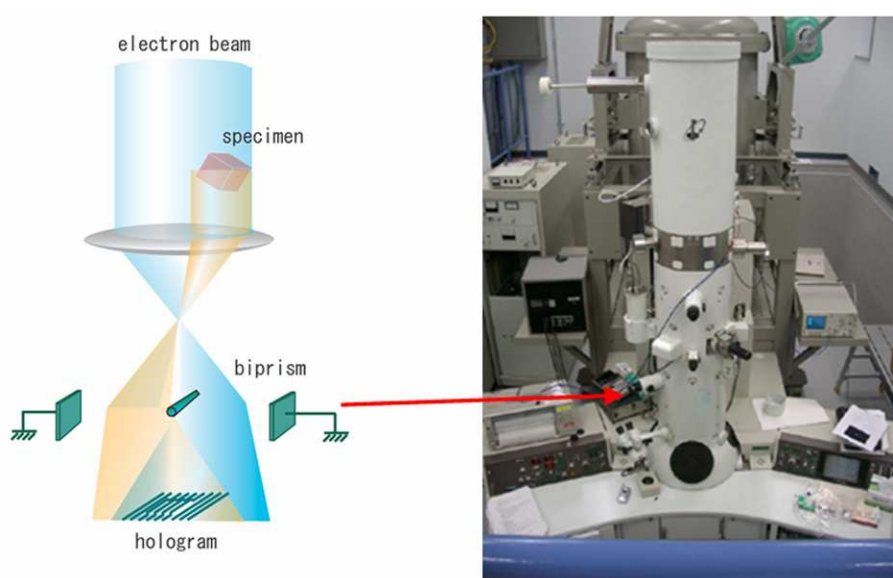


Fig. 1.2 Schematic of the electron holography and the image of a TEM equipped with a biprism.

The technique of off-axis electron holography basically depends on the interference of two (or more) coherent electron waves that combine to produce an interferogram or hologram. Off-axis electron holography involves two steps. The amplitude and phase distributions in the image plane of a TEM are first recorded in an electron hologram by interfering reference and object electron beams, and then reconstructed by an optical or digital procedure. To acquire an off-axis electron hologram, the region of interest on the specimen should be positioned to cover half the field of view. An electron hologram is produced by the application of voltage to the biprism with half of the electron wave passing through the vacuum as the reference wave and the other half of the electron wave passing through the specimen as the object wave. The amplitude and the phase distribution of the electron wave from the specimen are recorded in the intensity and the position of the holographic fringes, respectively.

The microscope geometry for off-axis electron holography in the TEM is schematically shown in Fig. 1.2. The specimen is illuminated with a defocused, coherent beam of electrons. Usually we need to adjust the condenser-lens stigmator

settings to make the incident illumination highly elliptical. The specimen is positioned to cover roughly half the field of view. The electron biprism consists of a conductive filament supplied with a voltage, and two grounded electrode platelets. The conductive filament is usually a thin ( $<1 \mu\text{m}$ ) metallic wire or quartz fiber coated with gold or platinum, which is biased by means of an external power supply or battery [22]. Although the biprism may be located at one of several alternative points along the beam path below the specimen, its usual and most conventional position is in place of one of the selected-area apertures. The interference-fringe spacing and the width of the fringe overlap region are determined by the biprism voltage and the specimen-lens geometry.

When the biprism is aligned to the  $y$  direction, the hologram is formed as a result of the interference between the object wave  $\Phi_o$  and the reference wave  $\Phi_r$  (Fig. 1.3), which are given by,

$$\Phi_o(x, y) = \phi_0(x, y) \exp\left[i\eta(x, y) + 2\pi i \frac{\alpha}{\lambda} x\right], \quad (1.1)$$

$$\Phi_r(x, y) = \exp\left[-2\pi i \frac{\alpha}{\lambda} x\right]. \quad (1.2)$$

Here  $x$  and  $y$  are coordinates in the hologram,  $\phi_0$  is amplitude,  $\eta$  is phase,  $\lambda$  is the electron wavelength, and the reference wave and object wave are tilted by an angle  $\alpha$ .

Thus, the image intensity of a conventional TEM image can be described as the modulus squared of an electron wave function:

$$I(x, y) = |\Phi_o(x, y)|^2 = \phi_0^2(x, y).$$

This function only records the amplitude distribution of the specimen.

However, the intensity distribution in an off-axis electron holography can be represented by the addition of a tilted plane reference wave to the tilted object wave, in the form,

$$\begin{aligned}
 I(x, y) &= |\Phi_o(x, y) + \Phi_r(x, y)|^2 \\
 &= 1 + \phi_0^2(x, y) + 2\phi_0(x, y) \cos\left(4\pi \frac{\alpha}{\lambda} x + \eta(x, y)\right)
 \end{aligned}
 \tag{1.3}$$

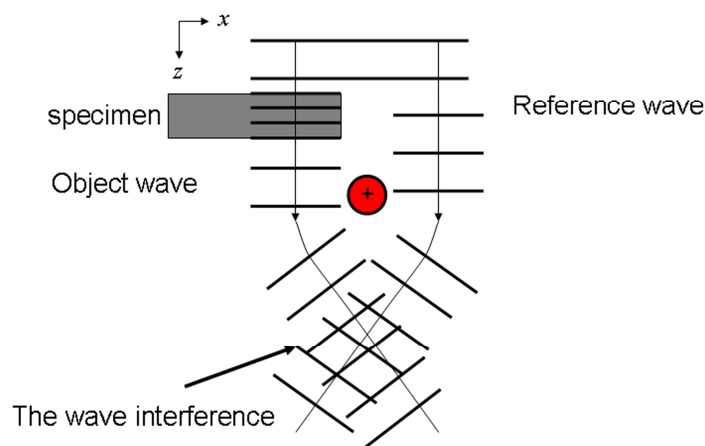


Fig. 1.3 Interference of the object wave and the reference wave.

Thus, the hologram will consist of a series of cosinusoidal fringes (the last term in the Eq. 1.3) superimposed onto the conventional bright-field image (i.e., the first two terms in the Eq.1.3). Any changes in the positions and/or spacing of the interference fringes will reflect the relative phase shift of the electron wave that has passed through different parts of the specimen. The phase term  $\eta(x, y)$  now is contained in the hologram image and can be separated from this image through a reconstruction procedure.

### 1.3.2 Hologram reconstruction

To obtain amplitude and phase information, by using the followed formula

$$\delta(q - Q) = \int_{-\infty}^{+\infty} \exp(2\pi i(q - Q)x) dx ,$$

the intensity of the recorded hologram is Fourier transformed. From Eq. (1.3), the complex Fourier transform of the hologram is given by

$$\begin{aligned} FT[I(x)] &= \delta(q) + \delta(q) \otimes FT[\phi_0^2(x)] \\ &+ \delta(q - 2Q) \otimes FT[\phi_0(x) \exp(i\eta(x))] \quad . \quad (1.4) \\ &+ \delta(q + 2Q) \otimes FT[\phi_0(x) \exp(-i\eta(x))] \end{aligned}$$

Equation (1.4) describes a peak at the reciprocal space origin corresponding to the Fourier transform of the reference image, a second peak centered on the origin corresponding to the Fourier transform of a bright-field TEM image of the specimen, a peak centered at  $q = -2Q$  corresponding to the Fourier transform of the desired image wave function, and a peak centered at  $q = +2Q$  corresponding to the Fourier transform of the complex conjugate of the wave function.

The reconstruction of a hologram to obtain amplitude and phase information is illustrated in Fig.1.4. Fig.1.4 (a) shows a hologram of a MgO crystal. To reconstruct the amplitude and the relative phase shift of the electron wave function, the hologram is firstly Fourier transformed, then one of the two sidebands is selected digitally and inversely Fourier transformed, as shown in Fig.1.4 (b)-(d). The amplitude and phase of this complex wave function are then easily calculated.

Via digital techniques, the phase is normally calculated modulo  $2\pi$  because of the cyclic property of the arctan function. Phase discontinuities of  $2\pi$  will appear at positions in the phase image at which the phase shift exceeds this amount. Such phase wraps can be misleading because they are unrelated to particular specimen features. Phase-unwrapping algorithms must then be used to ensure reliable interpretation of the image features. In addition, as noted above, it is standard practice to record reference holograms with the specimen removed. Any artifacts in the final hologram that are associated with local imperfections or irregularities of the imaging and recording systems can then be excluded by dividing the specimen wave function by the reference wave function.

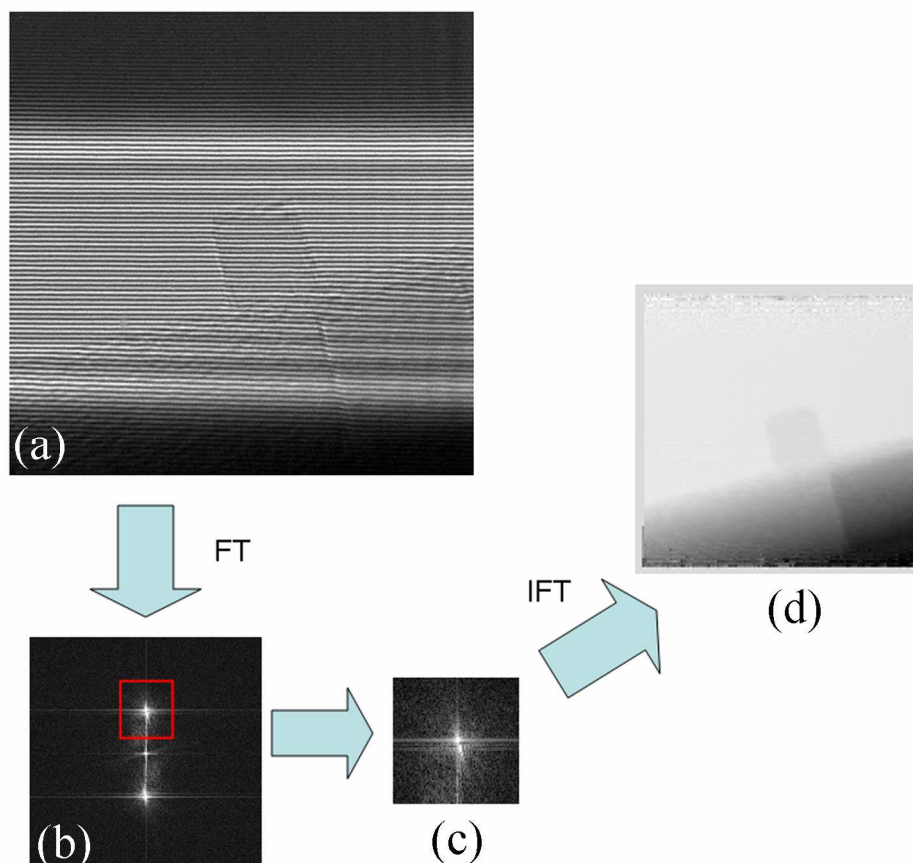


Fig. 1.4 (a) Off-axis electron hologram recorded from a MgO crystal; (b) Fourier transformation (FT) of the hologram; (c) The selected side band; (d) Reconstructed phase image after inverse Fourier transformation (IFT).

The reconstruction procedure with Fourier transformation is widely used in conventional electron holography. However, the spatial resolution of the reconstructed phase image is limited by the fringe spacing of the hologram [27-29], and is typically two or three times lower than the fringe spacing [30-34]. This happens because the center band and sidebands are mixed in the reconstruction procedure if the carrier frequency is small compared with the spatial frequency of the amplitude and phase of objects. However, if a high spatial carrier frequency is introduced to improve the resolution, a decrease in the fringe contrast will reduce the signal to noise ratio. Also, in the Fourier transformation method, if specimen has some edges or large phase variations, the Fourier spectrum of the specimen will extend widely not only in the side bands but also in the center band. There is no band filter that could perfectly

separate the side band with the center band; therefore, the reconstructed image will contain errors originating from the mixing of the diffraction components.

### 1.3.3 Phase shift by magnetic and electric fields

In general, for electric and magnetic fields given by the electric potential and the magnetic field, respectively, the phase change  $\eta$  of an electron wave that has passed through the specimen, relative to the wave that has passed only through vacuum, is given (in one dimension) by the expression [35]:

$$\eta(x) = C_E \int V(x, z) dz - \frac{e}{h} \iint B_{\perp}(x, z) dx dz, \quad (1.5)$$

where  $z$  is the incident electron beam direction,  $x$  is a direction in the plane of the specimen,  $V$  is the electronic potential of the specimen, and  $B_{\perp}$  is the component of the magnetic induction perpendicular to both  $x$  and  $z$ .

The interaction constant  $C_E$ , which depends on the energy of the incident electron beam, is given by the expression

$$C_E = \frac{2\pi}{\lambda E} \frac{E + E_0}{E + 2E_0}, \quad (1.6)$$

Where  $\lambda$  is the wavelength of the incident electron and  $E$  and  $E_0$  are the kinetic and rest mass electron energies, respectively.  $C_E$  has values of  $7.29 \times 10^6$ ,  $6.53 \times 10^6$ , and  $5.39 \times 10^6 \text{ rad} \cdot \text{V}^{-1} \cdot \text{m}^{-1}$  at 200kV, 300kV, and 1MV, respectively.

Mean inner potential (MIP)  $V_0$  is related to the composition and density of the specimen, and can be expressed by  $V_0 = \frac{1}{vol} \int_{vol} V_{atom}(x, y, z) dx dy dz$ , integrated over the object volume  $vol$ .

For situations in which neither  $V_0$  nor  $B$  varies with  $z$  within the specimen thickness  $t$ , and if one makes the simplifying assumption that any electric or magnetic fringing fields outside the specimen can be neglected, this expression for

the relative phase change can be simplified to

$$\eta(x) = C_E V_0(x)t(x) - \frac{e}{h} \int B_{\perp}(x)t(x)dx. \quad (1.7)$$

Differentiation of Eq. 1.7 with respect to  $x$  leads to an expression for the phase gradient of

$$\frac{d\eta(x)}{dx} = C_E \frac{d}{dx} [V_0(x)t(x)] - \frac{e}{h} B_{\perp}(x)t(x). \quad (1.8)$$

The Eq. 1.7 and Eq. 1.8 are fundamental to the measurement and quantification of electric and magnetic fields using electron holography for phase imaging.

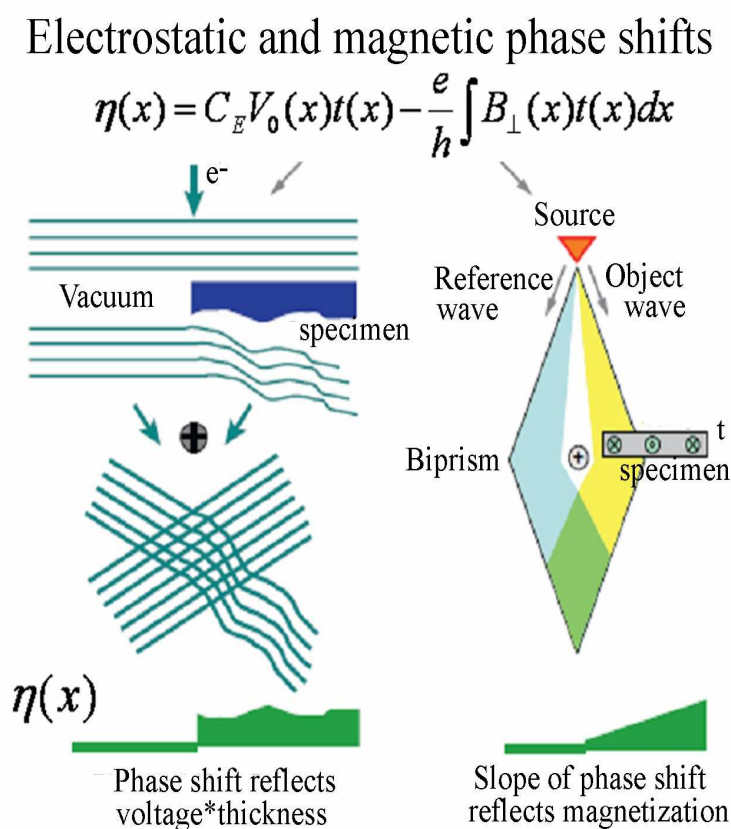


Fig. 1.5 Schematic illustrating of phase shift and phase gradients for electrostatic and magnetic fields [35].

The MIP term  $[V_0(x)t(x)]$  is likely to dominate both the phase and the phase gradient for cases in which the composition or the projected thickness of the specimen varies rapidly. If a specimen has uniform thickness and composition, the first term in Eq. 1.8 is zero. The phase gradient can then be interpreted directly and quantitatively in terms of the in-plane magnetic induction. Fig. 1.5 provides a schematic illustrating

of phase shift and phase gradients for electrostatic and magnetic fields, respectively.

For a non-magnetic specimen, rearrangement of equation above yields

$$V_0 = \left( \frac{1}{C_E} \right) \frac{d\eta(x)}{dx} / \frac{dt(x)}{dx}. \quad (1.9)$$

Thus, for a specimen of known thickness, such as a cleaved wedge, the MIP can be determined from measurement of the potential gradient, even when there are amorphous over-layers covering the specimen surfaces.

### 1.3.4 Applications of off-axis electron holography

Off-axis electron holography has been widely used in recent years to obtain phase distribution of electrostatic fields and magnetic fields. Several applications of the usage of off-axis electron holography are shown in Fig.1.6.

In Fig. 1.6 (a), off-axis electron holography has been used to measure two-dimensional electrostatic potentials in both unbiased and reverse biased silicon specimens that each contains a single *p-n* junction [36]. This technique also used to investigate magnetization reversal mechanisms and remanent states in exchange-biased submicron  $\text{Co}_{84}\text{Fe}_{16}/\text{Fe}_{54}\text{Mn}_{46}$  patterned elements [37], the relative results shown in Fig. 1.6 (b). In Fig. 1.6 (c), this technique determined the magnitude and spatial distribution of the electric field surrounding individual field-emitting carbon nanotubes [38]. In Fig.1.6 (d), the magnetic microstructure of a natural, finely exsolved intergrowth of submicron magnetite blocks is characterized by using off-axis electron holography in TEM. Single-domain and vortex states in individual blocks, as well as magnetostatic interaction fields between them, are imaged at a spatial resolution approaching the nanometer scale [39]. In Fig.1.6 (e), electron holography has been used to measure magnetic induction map of two double chains of magnetite crystals at room temperature [40].

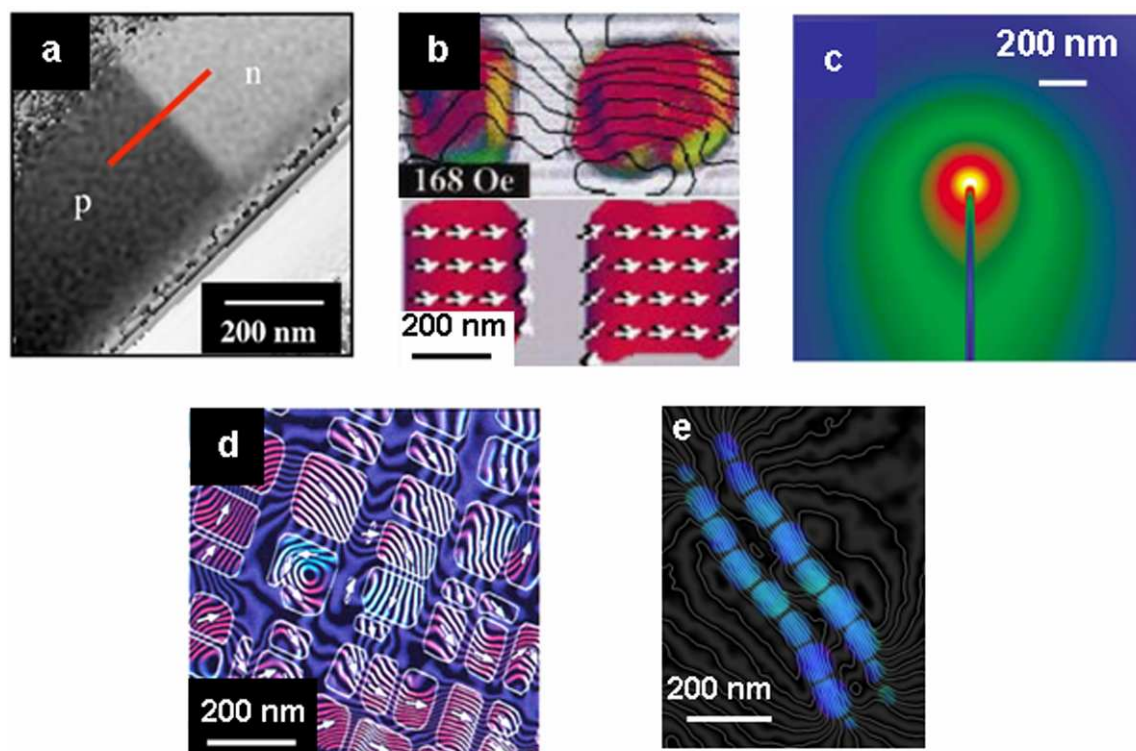


Fig.1.6 (a) Semiconductor physics: built-in voltage across a p-n junction; (b)Nanotechnology: Upper panel: remnant magnetic state in exchange-biased CoFe elements; Lower panel: micromagnetic simulation of the same elements; (c)Field Emission: Electrostatic potential from a biased carbon nanotube; (d)Geophysics: Evolved magnetite elements in the titan magnetite system; (e)Biophysics: Chains of magnetite crystals which grow in magnetotactic bacteria and are used for navigation.

#### 1.4 Other Forms of electron holography

A total of about twenty possible modes of electron holography, distinctly different in either their theoretical basis or their experimental requirements, may be available in recently research [25]. Here, we show phase-shifting electron holography briefly, as follows. This technique has an important advantage over conventional off-axis electron holography, and can provide a higher spatial resolution than conventional techniques based on the Fourier transformation.

Ru and colleagues [28, 41] have developed a phase-shifting reconstruction method for electron holography, in which a number of holograms with different initial phases

are acquired by slightly changing the angle of the incident electron beam, and thus in each hologram the interference fringes are displaced (phase-shifted) while the specimen position remains the same. The intensity at a certain point on a hologram will vary sinusoidally with the shift in the interference fringes. The phase and amplitude are then retrieved from the sinusoidal curve fitted to the intensity at each point.

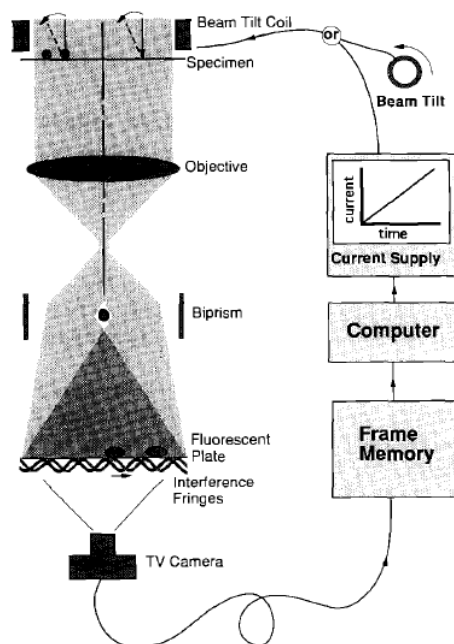


Fig. 1.7 Illustration of the experimental set up for phase-shifting electron holography [41].

Figure 1.7 shows an illustration of the experimental setup for phase-shifting electron holography. In this technique, a series of holograms whose interference fringes are shifted one after another is recorded. The shifting of the interference fringes is carried out by the incident electron wave, which corresponds to the shift of the initial phase difference between the object wave and the reference wave. As shown in the Fig. 1.7, when the incident electron wave is tilted to  $\theta_n$ , the intensity of the interference fringes is expressed by using the object wave  $\Phi_o$  and the reference wave  $\Phi_r$ , as

$$I(x, y, n) = |\Phi_o + \Phi_r|^2 \quad (1.10)$$

$$= 1 + |\phi_o(x, y)|^2 + 2\phi_o(x, y) \cos[2k\alpha x - \eta(x, y) + k\theta_n w]$$

where  $n$  is an integer numbering of the hologram,  $\phi_o(x, y)$  and  $\eta(x, y)$  are the amplitude and phase of the object wave, respectively,  $\alpha$  is the angle of the electron waves deflected by the electron biprism,  $w$  is the width of the interference area and  $k = 2\pi/\lambda$ , where  $\lambda$  is the wavelength. The phase term  $k\theta_n w$  is the initial phase difference between the object wave and the reference wave in the  $n$ th hologram. Therefore, the interference fringes are shifted by tilting the incident electron wave.

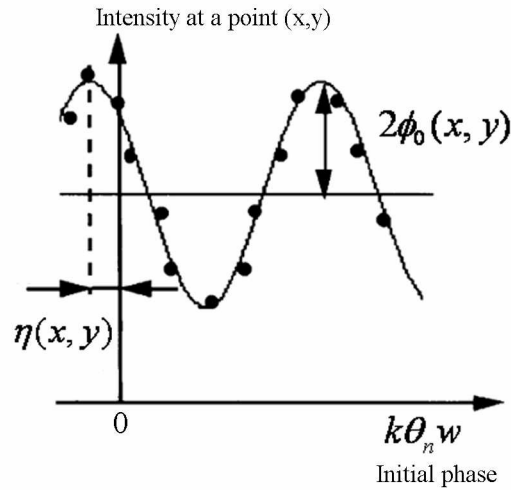


Fig. 1.8 Reconstruction of object wave at a certain point  $(x, y)$  [42].

The object wave is reconstructed from a series of holograms. The intensity at a certain point  $(x, y)$  on the holograms will vary sinusoidally by shifting interference fringes. Fig. 1.8 illustrates the plot of intensity as a function of the initial phase  $k\theta_n w$  [42]. The initial phase in each hologram is obtained from the phase value at the center of the sideband in the Fourier transform of the hologram. The plots are fitted using a cosine curve and the object wave,  $\phi_o(x, y)$  and  $c$ , is finally determined from the curve. Further details of phase-shifting electron holography have been described in these literatures [28, 41].

## 1.5 Other techniques for phase measurement

### 1.5.1 Phase measurement using the transport of intensity equation

Gabor proposed the electron holography technique, which is powerful for measuring both the phase and amplitude of the electron wave that passed through a specimen. However, holography cannot be applied to general cases, since there is a requirement for a vacuum region where the reference wave passes through. In 1983, Teague [43] proposed an equation for wave propagation in terms of phase and intensity distributions, and showed that the phase distribution may be determined by measuring only the intensity distributions. This equation is named as Transport of Intensity Equation (TIE). The TIE was recently applied successfully to TEM at medium resolution to observe static potential distributions of biological and non-biological specimens or to measure magnetic fields [44-46].

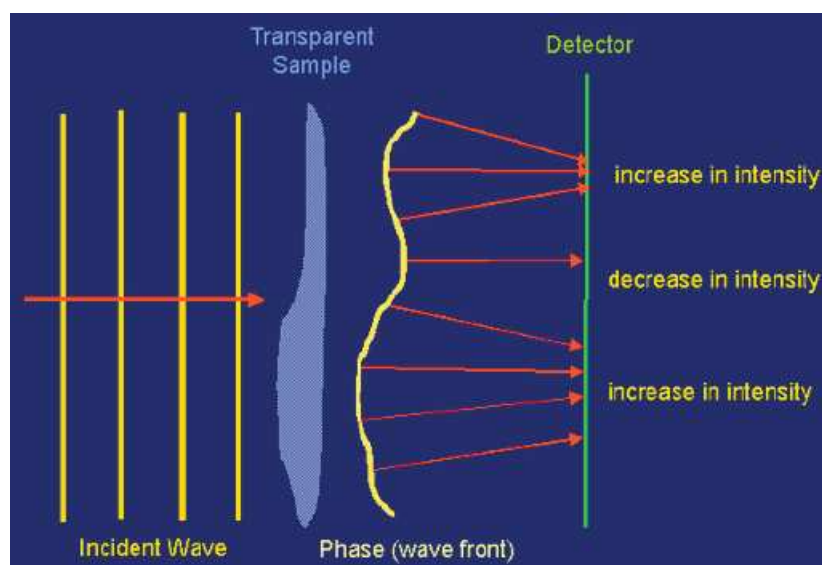


Fig.1.9 Schematic illustration of transport of intensity due to wave propagation [44].

The wave propagation is schematically shown in Fig. 1.9. When a plane wave is transmitted through a specimen, both the amplitude and the phase of the wave are modulated. For a phase object, the amplitude change is negligible, and the information concerning the specimen is encoded in the phase modulation only. Thus, the

amplitude of the exit wave is almost constant immediately below the specimen exit surface. However, when a modulated wave propagates through empty space, the amplitude at some places will increase and at other places the amplitude will decrease, according to the phase modulation induced by the specimen.

Mathematically, the TIE for electrons exactly corresponds to the Schrodinger equation for high-energy electrons in free space. Namely, the following TIE

$$\frac{2\pi}{\lambda} \frac{\partial}{\partial z} I(xyz) = -\nabla_{xy} \cdot (I(xyz) \nabla_{xy} \phi(xyz)), \quad (1.11)$$

is obtained,  $I$  and  $\phi$  are the intensity and phase distribution, respectively;  $x$  and  $y$  are the coordinates in the image plane,  $z$  is the vertical direction of the beam illumination.

Here,  $\frac{\partial I}{\partial z}$  is an intensity derivative along the wave propagation direction, and  $\nabla_{xy}^2$  is a two-dimensional Laplacian. For known boundary conditions and in the absence of intensity zeros (in-focus intensity), the TIE can be solved uniquely for the phase.

### 1.5.2 Phase measurement using Lorentz microscopy

Electron moving through a region of space with an electrostatic field and a magnetic field experiences the Lorentz force. The Lorentz force acts normal to the travel direction of the electron, a deflection will occur. The deflection angle is linked to the presence of electric or magnetic fields.

Lorentz microscopy is all about introducing controlled aberrations in the transfer function of the microscopy in order to induce visible contrast. There are two modes in Lorentz microscopy [47]: the Fresnel mode, in which you observe domain walls and magnetization ripples, and the Foucault mode, where domains are imaged.

The Fresnel mode: in conventional TEM, the minimum observed contrast indicates the in-focus position of the specimen. In this position, the domain walls do not appear. In the Fresnel mode, under-focusing or over-focusing is used to image the walls. A wall appears as a dark line when there is a diffusion of electrons, whereas it is white when there is an accumulation of electrons (Fig.1.10). It is then possible to follow the

domain wall motion under the application of an external magnetic field. It gives essentially qualitative information.

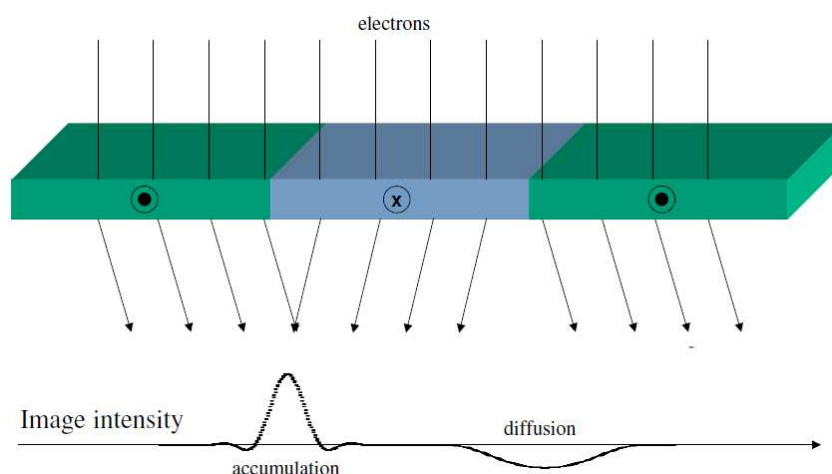


Fig.1.10 Schematic of the electron path through a magnetic specimen in Fresnel mode.

The Foucault mode: this mode corresponds to a bright field image mode in conventional TEM. This means that you select a part of your beam with an aperture located in the back focal plane of your imaging lens. The electrons that pass through the aperture will appear bright whereas the others will appear dark. The deflection angles linked to magnetization are small and you cannot really differentiate them from the transmitted beam, you have to put the aperture quite close to the transmitted beam. Getting nice results in this mode is therefore trickier than getting data from the Fresnel mode.

Lorentz microscopy is a way to visualize some information related to magnetic or electric structures. It requires the introduction of controlled aberrations in the microscope transfer function in order to induce contrast. However, Lorentz microscopy is only semi-quantitative, and to extract some quantitative physical information a perfect knowledge of the electron-optical set up is needed.

## 1.6 Aims and contents in this thesis

In conventional off-axis electron holography based on Fourier transformation method, the spatial resolution of the reconstructed phase image is limited by the fringe spacing. However, the aim of this research is to develop a new method which can overcome the limitation between the spatial resolution and the fringe spacing. Under the use of a stage-scanning system, a stage-scanning electron holography is proposed which has the property to overcome the limitation mentioned above. Based on the stage-scanning electron holography, a technique of super-resolution phase reconstruction is presented for improving the spatial resolution of the reconstructed phase image.

There are five chapters in this thesis, which are organized as follows:

In this first chapter, the outline and history of electron holography, basic knowledge of off-axis electron holography and reconstruction procedure based on Fourier transformation method; other forms of electron holography as well as other method for phase measurement and the aim of this thesis are described.

In the second chapter, a stage-scanning electron holography technique is proposed, which can directly acquire an interferogram, that is, cosine image of phase distribution. The interferogram is constructed by shifting the specimen in one direction with a stage-scanning system and acquiring line intensities of holograms. Under phase object approximation, the object phase can be readily obtained from the interferogram without any reconstruction procedure. The spatial resolution of phase is determined independently of the fringe spacing, overcoming the limitation of conventional techniques based on the Fourier transformation method.

In the third chapter, the stage-scanning electron holography is improved and extended for non-phase object. The resolution improvement is also demonstrated by observing cobalt nanoparticles through comparing the stage-scanning holography and the conventional holography, and significantly sharper images were obtained with the former technique.

In the fourth chapter, a super-resolution reconstruction technique is introduced into

stage-scanning electron holography when the scan step of the stage-scanning is a sub-pixel distance. The process of the acquired series of holograms with sub-pixel specimen shift results in a higher pixel density and spatial resolution as compared to the phase image obtained with conventional holography. The final resolution exceeds the limit of the CCD pixel size divided by the magnification.

The fifth chapter contains the general conclusions of this thesis.

## Reference

- [1] D. B. Williams and C. B. Carter (1996) Transmission electron microscopy: A textbook for materials science. Plenum press, New York and London.
- [2] E. Ruska (translated by T. Mulvey) (1980) The early development of electron lenses and electron microscopy. Stuttgart, Hirzel.
- [3] M. M. Freundlich (1963) Origin of the electron microscope. *Science* **142**: 185-188.
- [4] E. Ruska (1986) Nobel lecture.
- [5] B. Voutou and E. C. Stefanaki (2008) Electron microscopy: The basics. Physics of advanced materials winter school.
- [6] A. Delong, K. Hladil, V. Kolarik and P. Pavelka (2000) Low voltage electron microscope 1. Design, 2. Application, 3. Present and future possibilities. *EUREM 12*.
- [7] A. M. Glauert (1974) The high voltage electron microscope in biology. *J. cell. boil.* **63**:717-748.
- [8] [http://en.wikipedia.org/wiki/File:Scheme\\_TEM\\_en.svg](http://en.wikipedia.org/wiki/File:Scheme_TEM_en.svg).
- [9] B. Fultz and J. Howe (2007) Transmission electron microscopy and diffractometry of materials. Springer.
- [10] P. E. Champness (2001) Electron diffraction in the transmission electron microscope. Garland Science.
- [11] A. Hubbard (1995) The handbook of surface imaging and visualization. CRC Press.
- [12] R. Egerton (2005) Physical principles of electron microscopy. Springer.
- [13] E. Kirkland (1998) Advanced computing in electron microscopy. Springer.
- [14] R. F. Egerton (1996) Electron energy-loss spectroscopy in the electron microscope. Springer.
- [15] J. M. Cowley and A. F. Moodie (1957) The scattering of electrons by atoms and crystals. A new theoretical approach. *Acta Crystallographica*. **199(3)**: 609-619.
- [16] A. Tonomura (1992) Electron –holographic interference microscopy, *Adv. Phys.* **41**: 59-103.
- [17] H. Lichte (1991) Electron image plane off-axis holography of atomic structure.

*Adv. Opt. Electron Microsc.* **12**: 25-91.

[18] D. Gabor (1948) A new microscopic principle, *Nature* **161**: 777-778.

[19] D. Gabor (1949) Microscopy by reconstructed wave-fronts, *Proc.R.Soc. A.* **197**:454-87.

[20] M. E. Haine and T. Mulvey (1952) The formation of diffraction image with electrons in the Gabor diffraction microscope, *J.Opt.Soc.Am.* **42**: 763.

[21] E. H. Leith and J. Upatnieks (1962) Reconstructed wavefronts and communication theory, *J.Opt.Soc.Am.* **52**: 1123-30.

[22] H. Lichte and M. Lehmann (2008) Electron holography-basics and applications, *Rep. Prog. Phys.* **71**:016102.

[23] G. Möllenstedt and H. Wahl (1968) Elektronenholographie und Rekonstruktion mit Laserlicht, *Naturwissenschaften* **55**: 340-1.

[24] H. Wahl (1975) Bildebenen holographie mit Elektronen *Thesis* University of Tübingen.

[25] J M Cowley (1992) Twenty forms of electron holography, *Ultramicroscopy* **41**: 335-348.

[26] A. Tonomura, T. Matsuda, J. Endo, H. Todokoro and T. Komoda (1979) Development of field-emission electron microscope, *J. Electron Microsc.* **28**:1-11.

[27] T. Fujita, K. Yamamoto, M. R. McCartney, and D. J. Smith (2006) Reconstruction technique for off-axis electron holography using coarse fringes. *Ultramicroscopy* **106**: 486-491.

[28] Q. Ru, J. Endo, T. Tanji and A. Tonomura (1991). Phase-shifting electron holography by beam tilting. *Appl Phys Lett* **59**: 2372.

[29] G. Lai, Q. Ru, K. Aoyama and A. Tonomura (1994). Electron-wave phase-shifting interferometry in transmission electron microscopy. *J Appl Phys* **76**: 39.

[30] W. J. de Ruijter, J.K. Weiss (1993) Detection limits in quantitative off-axis electron holography. *Ultramicroscopy* **50**: 269.

[31] K. Yamamoto, T. Hirayama, T. Tanji (2004). Off-axis electron holography without Fresnel fringes. *Ultramicroscopy* **101**: 265-269.

[32] K. Yamamoto, Y. Sugawara, M. R. McCartney and D. J. Smith (2010).

Phase-shifting electron holography for atomic image reconstruction. *J. Electron Microsc.* **59**: s81-s88.

[33] K. Harada, A. Tonomura, T. Matsuda, T. Akashi and Y. Togawa (2004). High-resolution observation by double-biprism electron holography. *J Appl Phys* **96**: 6097.

[34] H. Lichte, M. Linck, D. Geiger and M. Lehmann (2010). Aberration correction and electron holography. *Microsc Microanal* **16**:434-440.

[35] M. R. McCartney and D. J. Smith (2007) Electron holography: Phase imaging with nanometer resolution, *Annu. Rev. Mater. Res.* **37**:729-767.

[36] A. C. Twitchett, R. E. Dunin-Borkowski, R. J. Hallifax, R. F. Broom and P. A. Midgley (2003) Off-axis electron holography of electrostatic potentials in unbiased and reverse biased focused ion beam milled semiconductor devices, *J. Microscopy* **214**: 287-296.

[37] R. E. Dunin-Borkowski, M. R. McCartney, B. kardynal, M. R. Scheinfein and D. J. Smith (2001) Off-axis electron holography of exchange-biased CoFe/FeMn patterned nanostructures, *J. Appl. Phys.* **90**:2899.

[38] J. Cumings and A. Zettl (2002) Electron holography of field-emitting carbon nanotubes, *Phys. Rev. Lett.* **88**: 056804.

[39] R. J. Harrison, R. E. Dunin-Borkowski and A. Putnis (2002) Direct imaging of nanoscale interactions in minerals, *Proc. Nat. Acad. Sci.* **99**:16556-16561.

[40] E. T. Simpson, T. Kasama, M. P'osfai, P. R. Buseck, R. J. Harrison and R. E. Dunin-Borkowski (2005) Magnetic induction mapping of magnetite chains in magnetotactic bacteria at room temperature and close to the Verwey transition using electron holography, *J. Phys. Conf. Ser.* **17**: 108-121.

[41] Q. Ru, G. Lai, K. Aoyama, J. Endo and A. Tonomura (1994) Principle and application of phase-shifting electron holography. *Ultramicroscopy.* **55**: 209-220.

[42] K. Yamamoto, T. Hirayama, T. Tanji and M. Hibino (2003) Evaluation of high-precision phase-shifting electron holography by using hologram simulation. *Surf. Interface Anal.* **35**: 60-65.

[43] M. R. Teague (1983) Deterministic phase retrieval: a Green's function solution. *J.*

*Opt. Soc. Am* **73**:1434-1441.

[44] K. Ishizuka and B. Allman (2005) Phase measurement in electron microscopy using the transport of intensity equation, *Microscopy Today*, 22-24.

[45] M. R. Teague, (1983) Deterministic phase retrieval: a Green's function solution, *J. Opt. Soc. Am.* **73**:1434-1441.

[46] T. C. Petersen, V. J. Keast, K. Johnson and S. Duvall (2007) TEM-based phase retrieval of p-n junction wafers using the transport of intensity equation, *Philosophical Magazine*, **87**: 3565-3578.

[47] M. D Graef (2009) Recent progress in Lorentz transmission electron microscopy, *ESOMAT*, 01002.

## **Chapter 2 Development of stage-scanning electron holography**

### **2.1 Introduction**

Electron holography is a powerful transmission electron microscopy technique [1-5], which yields quantitative information on the phase and amplitude of electrons passed through a specimen with high spatial resolution, whereas only the intensity distribution can be obtained with conventional electron microscopy. Since the development of the field emission gun and the electron biprism, electron holography has been a popular technique of probing the spatial distribution of electric or magnetic field [6-9]. In electron holography, the amplitude and phase distributions are first recorded in an electron hologram and then reconstructed by an optical or digital reconstruction system. Reconstruction procedures involving Fourier transformation are widely used to extract the phase and amplitude information; in these procedures the electron hologram is Fourier transformed, and then the selected sideband is inversely Fourier transformed. A serious drawback of this procedure [10-14] is that the spatial resolution of the reconstructed electron holography image is limited by the fringe spacing of the hologram. Generally, the fringe spacing should be narrower than one-third of the spatial resolution required in the reconstructed image. Efforts have been made to make fringes narrower to improve the resolution; however, this results in coherence loss.

In this chapter, a technique is proposed which can directly acquire an interferogram, that is, cosine image of phase, by moving the specimen and recording line intensities in the hologram at different object positions. The resultant image becomes an interferogram that provides the phase distribution under phase object approximation. Taking line intensities eliminates the carrier fringes in the holograms and yields the

interferogram. Under a phase object approximation, a phase image can be easily obtained from the interferogram without Fourier transformation.

## 2.2 Development of stage-scanning electron holography

### 2.2.1 Principle and experimental methods

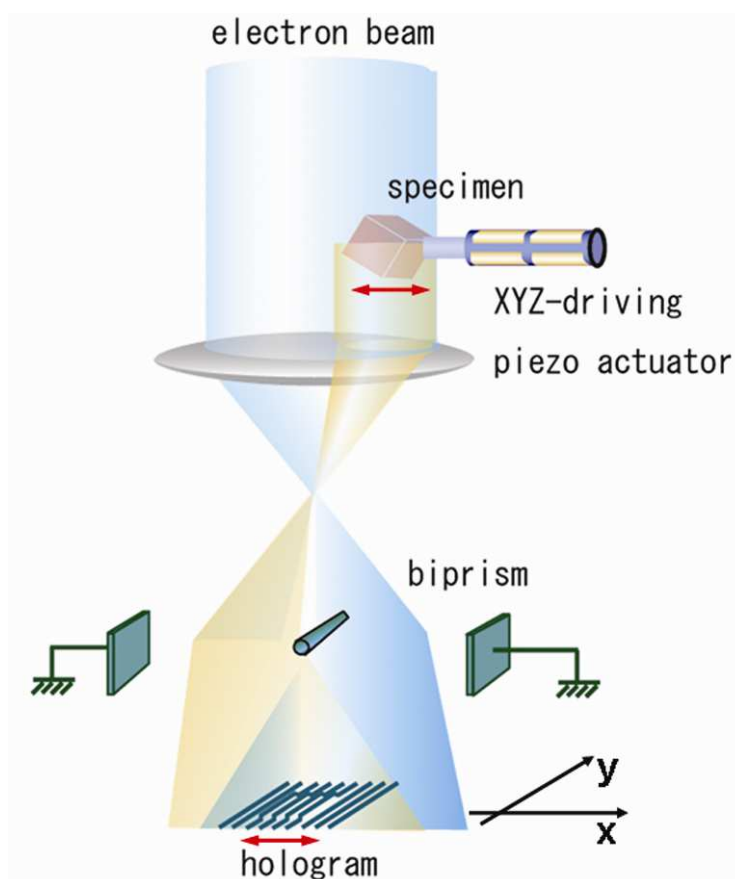


Fig.2.1 Schematic of electron holography with a stage-scanning specimen holder.

Figure 2.1 schematically shows the electron optics and instruments used in the stage-scanning holography method. A collimated electron beam illuminates the specimen which is positioned to cover half the field of view. Application of a voltage to the electron biprism located below the specimen results in an overlap of the object wave passing through the specimen with a reference wave passing through the vacuum. A stage-scanning system [15-17] is employed, which comprises a specially designed TEM specimen holder equipped with a piezo-driven specimen stage. This

system enables three-dimensional (3D) scanning of the specimen in a fixed electron optics configuration and has been used for scanning confocal electron microscopy in a conventional transmission electron microscope. Figure 2.2 (a) shows a photograph of the holder head. A tubular piezoelectric actuator is used for moving the stage. Figure 2.2 (b) shows a schematic of the stage-scanning system, which includes the specimen holder, power supply and control program running on a PC.

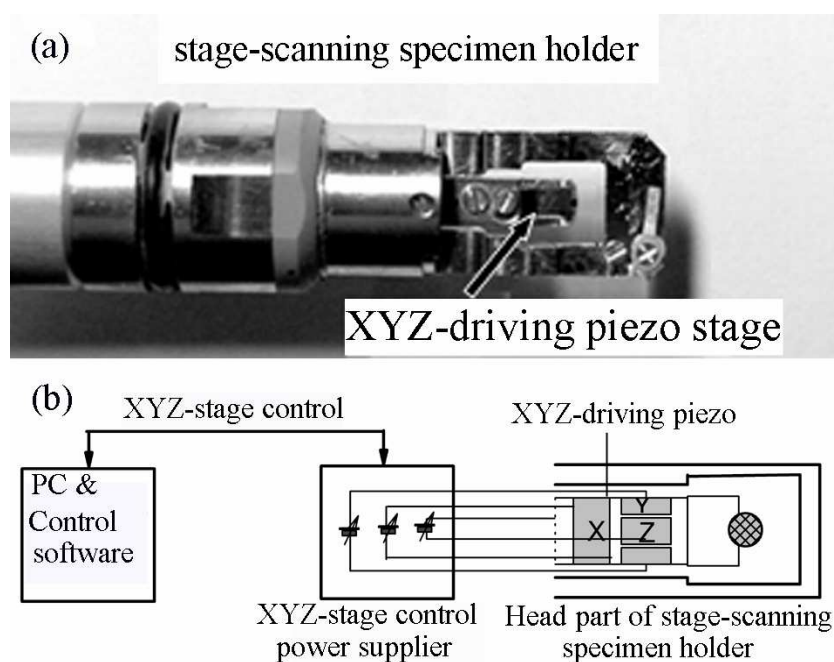


Fig.2.2 (a) Head of the specially designed TEM specimen holder; (b) schematic of the stage-scanning system comprising the specimen holder, power supply and control unit.

When the biprism is aligned to the  $y$  direction, the hologram is formed as a result of the interference between the object wave  $\Phi_o$  and the reference wave  $\Phi_r$ , which are given by

$$\Phi_o(n, x, y) = \phi_0(x - n\Delta x, y) \exp[i\eta(x - n\Delta x, y)], \quad (2.1)$$

$$\Phi_r(x, y) = \exp\left[2\pi i \frac{\alpha}{\lambda} x\right]. \quad (2.2)$$

Here  $x$  and  $y$  are coordinates in the hologram,  $\phi_0$  is amplitude,  $\eta$  is phase,  $\Delta x$

is the scan step width of the specimen movement in the  $x$  direction,  $n$  is the step number,  $\lambda$  is the electron wavelength, and the reference wave is tilted by an angle  $\alpha$  relative to the object wave. The hologram intensity is expressed by

$$I(n, x, y) = |\phi_0(x - n\Delta x, y)|^2 + 1 + 2\phi_0(x - n\Delta x, y) \cos\left[\eta(x - n\Delta x, y) + 2\pi \frac{x}{m}\right], \quad (2.3)$$

here  $m$  refers to the fringe spacing, which corresponds to  $\frac{\lambda}{\alpha}$ .

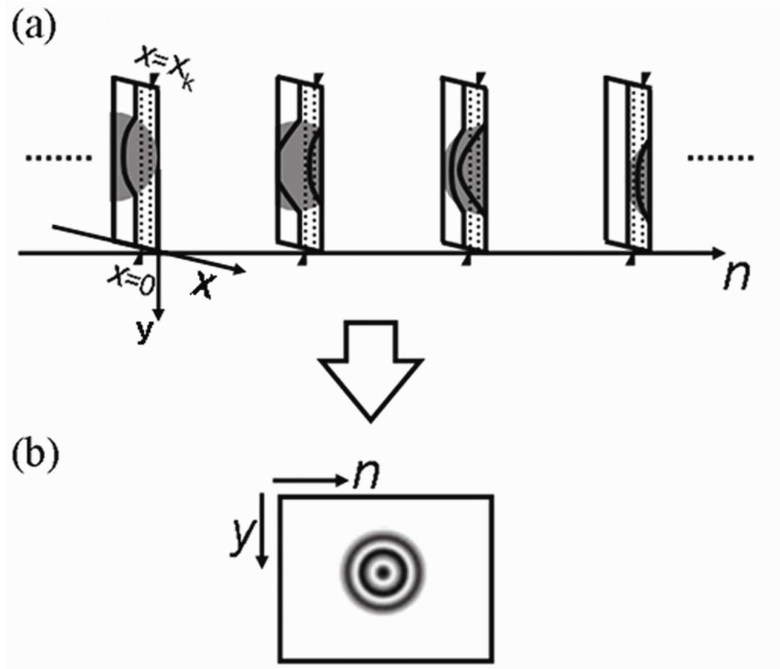


Fig. 2.3 (a) A series of holograms in which only one line intensities at  $x=0$  are captured; (b) the interferogram (cosine image of phase distribution) reconstructed from the line intensities in the holograms.

Assuming that line intensities in each hologram are captured at  $x=0$  in the hologram plane, as schematically shown in Fig. 2.3 (a), the line intensities along the  $y$  axis in the hologram with  $n$ -th specimen position are expressed by

$$\Pi(n, y) = |\phi_0(-n\Delta x, y)|^2 + 1 + 2\phi_0(-n\Delta x, y) \cos[\eta(-n\Delta x, y)]. \quad (2.4)$$

After the specimen scan is completed, Eq. (2.4) can be viewed as the interferogram in the  $(-n\Delta x, y)$  plane, in which the carrier fringe no longer exists, as schematically shown in Fig. 2.3 (b). Under phase object approximation, where the amplitude

change is negligible, the amplitude  $\phi_0(-n\Delta x, y)$  can be replaced by 1 and the phase  $\eta(-n\Delta x, y)$  can be calculated as

$$\eta(-n\Delta x, y) = \cos^{-1}\left(\frac{1}{2}\Pi(n, y) - 1\right). \quad (2.5)$$

As the line intensities in each hologram along a fixed line  $x=0$  are recorded during the scan, the phase of this line can be obtained from Eq. (2.5) under phase object approximation, and the phase image can be easily reconstructed with a computer. This procedure does not use Fourier transformation, and therefore its spatial resolution is only limited by the scan step width and microscope resolution, not by the fringe spacing.

A JEOL JEM-ARM200F microscope equipped with a biprism was used for testing the proposed technique at an accelerating voltage of 200 kV. The “STEM Diffraction Imaging” software of Gatan Inc. was used to control the holder and acquire holograms.

### 2.2.2 Results and discussion

To give an outline of the proposed stage-scanning holography technique, Figure 2.4 presents an example of observing phase distribution, where a MgO crystal (Fig. 2.4(a)) was used as a testing sample. Figure 2.4(b) shows a hologram during acquisition. The holograms from different specimen positions were acquired and saved as a 3D data cube with the size of 95 pixels $\times$ 180 pixels $\times$ 80 steps. The total acquisition time in the present experiment was about 1min. 30 s including data transfer time and 1 second exposure time for each scan step. The interferogram was obtained by slicing the cube at a fixed position parallel to the biprism, as indicated by the red line in Fig. 2.4(b). The phase image can readily be obtained by Eq. (2.5) under phase object approximation, as shown in Fig. 2.4(c). In this example, phase changes of about  $2\pi$  due to the thickness variation can be observed. Here the 3D data cube was acquired first and sliced afterwards, however the interferogram (i.e. the phase image) can be

obtained in situ using the line CCD intensities at marked positions by lining up the line intensities side by side as the scan goes on. (Although the acquisition speed is still limited by the exposure time.) This example illustrates that the phase can readily be obtained by a single scan of the specimen.

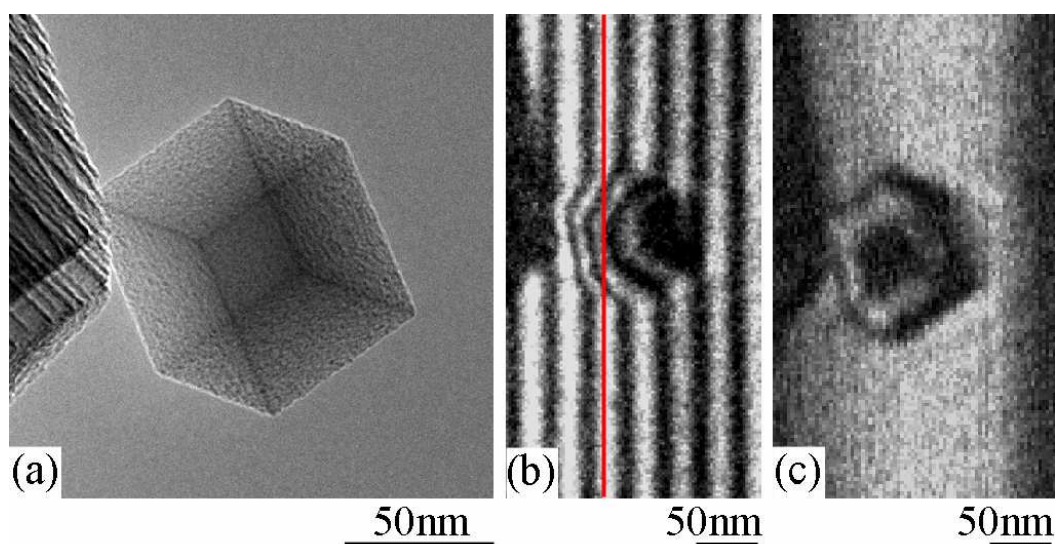


Fig.2.4 (a) TEM image of the MgO crystal; (b) a hologram extracted from the 3D data cube of holograms, an interferogram is obtained by slicing the 3D data cube along the red line; (c) the phase image obtained from the interferogram.

Another example of MgO crystal is presented in Fig. 2.5. In this example, phase changes of about  $6\pi$  due to the thickness variation can be observed despite a slight bending of the phase profiles due to the specimen drift. The interferogram (i.e. the phase image) can be obtained in situ using the line CCD intensities at marked positions by lining up the line intensities side by side as the scan goes on.

In this method, the intensity in each hologram along a fixed line  $x=0$  is recorded. As the line intensities are recorded during the scan, the phase of this line can be obtained from Eq. (2.5) under phase object approximation, and the phase image can be easily reconstructed with a computer. Since the reconstruction procedure is simple and the amount of data transferred from the CCD to the computer is small (1-dimensional array); the proposed technique is fast and can be applied to real-time

phase acquisition. Furthermore, this procedure does not use Fourier transformation, and therefore its spatial resolution is only limited by the scan step and microscope resolution, but not by the fringe spacing. An isotropic resolution can be achieved if the scan step is equal to the CCD pixel size divided by the magnification.

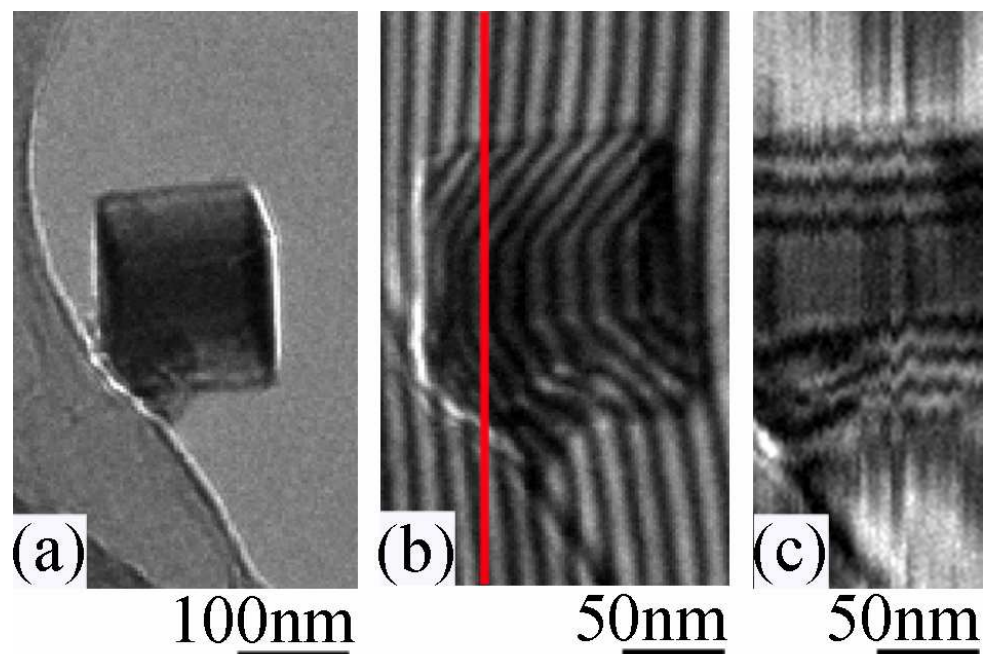


Fig. 2.5 (a) TEM image of the MgO crystal with tilted [110] incidence; (b) a hologram extracted from the 3D data cube of holograms, an interferogram is obtained by slicing the 3D data cube along the red line; (c) the phase image obtained from the interferogram.

The total time needed for the simple phase acquisition method depends on the exposure time and the number of scan steps. In conventional holography, the total acquisition time of a  $n \times n$  pixel hologram is a sum of the exposure time and data transfer time from CCD to computer. In contrast, our technique uses one line ( $1 \times n$  pixels) signal per hologram, where  $n$  is the number of pixels along the  $y$  direction. Thus the total acquisition time becomes (exposure time)  $\times$  (number of scan steps) plus data transfer time and is longer than that in the conventional technique. This drawback can be partially compensated if we converge the electron beam to the line while keeping parallel illumination, or if we use several lines of CCD simultaneously and

average the obtained phase images from each line to reduce the exposure time at a given electron beam intensity and signal to noise ratio. In practice, because the resolution does not depend on the fringe spacing, a wider interference fringe which has a higher contrast can be used for reconstruction. Thus, the exposure time can be reduced for achieving the same signal to noise ratio.

### 2.3 Stage-scanning electron holography with a digital aperture

In the above section, a 3D data cube was recorded and sliced at a fixed position to form an interferogram, which was the cosine image of phase distribution. However, there is another method which also is possible for acquisition of the phase distribution. In this case, a 4D data cube of the holograms is recorded on which the specimen has different positions and then the phase information is separated through a digital aperture from the 4D data cube. Detailed information of this method is as follows.

#### 2.3.1 Methods

Electron waves passing through the specimen and vacuum regions are deflected by the electrostatic potential around the biprism so that an electron hologram is formed on the image plane. With the 2D movement of the specimen in the object plane, 2D holograms can be obtained, resulting in a 4D data array that can be expressed as

$$I(n_x, n_y, x, y) = \left| \phi_0(x - n_x \Delta x, y - n_y \Delta y) \right|^2 + 1 + 2\phi_0(x - n_x \Delta x, y - n_y \Delta y) \cos \left[ \eta(x - n_x \Delta x, y - n_y \Delta y) + 2\pi \frac{x}{m_x} + 2\pi \frac{y}{m_y} \right]. \quad (2.6)$$

Here  $x$  and  $y$  denote the position in a hologram,  $\phi_0$  and  $\eta$  are the amplitude and phase, respectively,  $m_x$  and  $m_y$  refer to the fringe spacing along the  $x$  and  $y$  directions, respectively,  $\Delta x$  and  $\Delta y$  are the scan steps and  $n_x$  and  $n_y$  are their indexes for the  $x$  and  $y$  directions, respectively.

By applying a pinhole aperture to the origin ( $x=0, y=0$ ) of holograms recorded at different specimen positions, an interferogram can be obtained as

$$I(n_x, n_y, 0, 0) = \left| \phi_0(-n_x \Delta x, -n_y \Delta y) \right|^2 + 1 + 2\phi_0(-n_x \Delta x, -n_y \Delta y) \cos[\eta(-n_x \Delta x, -n_y \Delta y)]. \quad (2.7)$$

Under the phase object approximation, the phase distribution can be easily calculated from the interferogram.

### 2.3.2 Results and disctssion

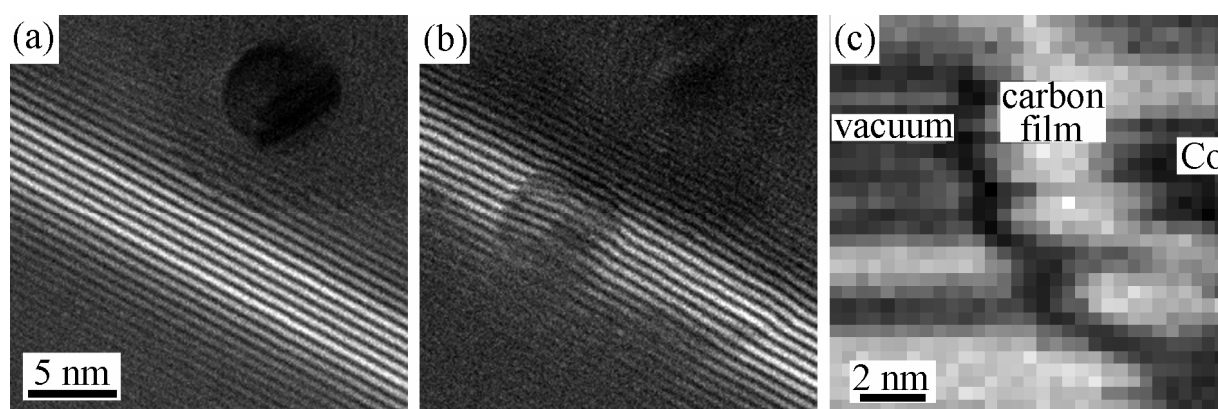


Fig. 2.6 Two extracted holograms of the Co particle (a) and (b), the specimen was moved from the position in hologram (a) to the position in hologram (b) using the scanning stage; (c) The interferogram which corresponds to the phase distribution.

Figures 2.6(a) and (b) show two holograms recorded for two positions of a Co particle with a diameter of 6 nm on an amorphous carbon film. The particle was moved into the fringe area and shifted the fringes as observed in Fig. 2.6(b). The fringe spacing is 0.6 nm in both holograms.

By applying the digital aperture to the center of each hologram, an interferogram was obtained as shown in Fig. 2.6(c). The particle can be observed in this interferogram. According to Eq. 2.7, this interferogram corresponds to the phase distribution of the specimen. The phase change from the vacuum to the carbon film was approximately  $\pi$ , corresponding to the fringe contrast change from black to white. The two horizontal stripes observed at the lower part of the image originate from the

biprism drift during the acquisition.

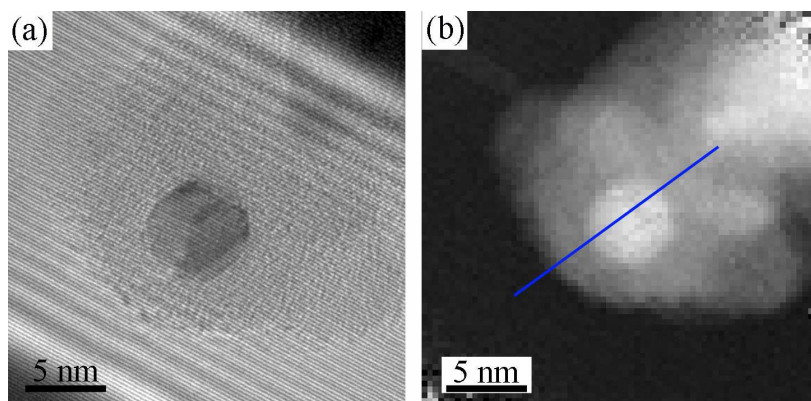


Fig. 2.7 (a) Electron hologram of the Co particle obtained by conventional electron holography; (b) phase image of the Co particle reconstructed from the hologram (a).

For comparison, the phase of the same particle was obtained by conventional electron holography using the Fourier transformation reconstruction method. Fig. 2.7 (a) shows the hologram recorded by conventional holography of the Co particle. In conventional electron holography, due to the limitation between spatial resolution and fringe spacing, a finer fringe spacing of 0.2 nm was used. A hologram without specimen was taken as a reference. Figure 2.7(b) shows the reconstructed phase image from the hologram of the Co particle.

Figure 2.8 shows the phase change profile obtained by conventional electron holography. The phase change was 3.2 radians from vacuum to the carbon film, and 3.5 radians from the carbon film to the center of the Co particle, which agrees with the phase change observed in Fig. 2.6(c). The result demonstrates the successful acquisition of the phase distribution by the new method.

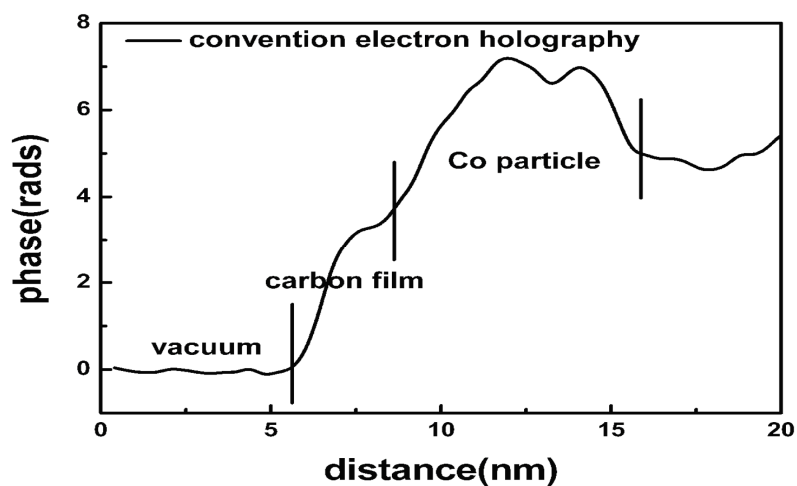


Fig.2.8 Line profile of the measured phase shift across the Co particle using conventional electron holography.

## 2.4 Conclusions

An electron holography technique was proposed in this chapter. Through the technique an interferogram can be obtained using line intensities in holograms acquired at different specimen positions. The resultant interferogram corresponds to the object phase under phase object approximation. This technique yields the phase distribution without the use of Fourier transformation, and therefore the spatial resolution can be determined independently of the fringe spacing in the holograms. Experimental results for MgO crystals demonstrated the practicability and reliability of this technique.

## Reference

- [1] A. Tonomura (1992) Electron –holographic interference microscopy, *Adv. Phys.* **41**: 59-103.
- [2] H. Lichte and M. Lehmann (2008) Electron holography-basics and applications, *Rep. Prog. Phys.* **71**:016102.
- [3] A. Tonomura (1987) *Rev Mod Phys.* **59**:639-69.
- [4] A. Tonomura, T. Matsuda, J. Endo, H. Todokoro and T. Komoda (1979) *J Electron Microsc.* **28**:1-11.
- [5] D. Gabor (1949) Proc. R. Soc. London, Ser. A **197**: 454.
- [6] W. J. de Ruijter (1995) Imaging properties and applications of slow-scan charge-coupled-device cameras suitable for electron microscopy, *Micron* **26**: 247-75.
- [7] W. J. de Ruijter, J. K. Weiss (1993) Detection limits in quantitative off-axis electron holography, *Ultramicroscopy* **50**:269-83.
- [8] D. J. Smith, W. J. de Ruijter, J. K. Weiss and M. R. McCartney (1999) Quantitative electron holography. In introduction to electron holography, ed. E Volkl, LF Allard, DC Joy, pp. 1107-24, New York: Kluwer.
- [9] A. Tonomura, T. Matsuda, J. Endo, H. Todokoro and T. Komoda (1979) Development of field-emission electron microscope, *J. Electron Microsc* **28**: 1-11.
- [10] T. Fujita, K. Yamamoto, M. R. McCartney and D. J. Smith (2006) Reconstruction technique for off-axis electron holography using coarse fringes, *Ultramicroscopy* **106**: 486-491.
- [11] K. Yamamoto, T. Hirayama, T. Tanji (2004) Off-axis electron holography without Fresnel fringes, *Ultramicroscopy* **101**: 265-269.
- [12] Q. Ru, J. Endo, T. Tanji and A. Tonomura (1991) Phase-shifting electron holography by beam tilting, *Appl. Phys. Lett.* **59**:2372.
- [13] Qingxin Ru, Tsukasa Hireyama, Junji Endo and Akira Tonomura (1992) Hologram-shifting method for high-speed electron hologram reconstruction, *Jpn. J. Appl. Phys.* **31** :1919-1921.

- [14] Q. Ru, G. Lai, K. Aoyama, J. Endo and A. Tonomura (1994) Principle and application of phase-shifting electron holography, *Ultramicroscopy* **55**: 209-220.
- [15] Takeguchi M, Shimojo M, Tanaka M, Che R, Zhang W and Furuya K (2006) Electron holographic study of the effect of contact resistance of connected nanowires on resistivity measurement. *Surf Interface Anal.* **38**: 1628-1631.
- [16] M. Takeguchi, K. Mitsuishi, D. Lei and M. Shimojo (2011) Development of sample-scanning electron holography, *Microsc Microanal.* **17**(Suppl 2):1230.
- [17] Takeguchi M, Hashimoto A, Shimojo M, Mitsuishi K and Furuya K (2008) Development of a stage-scanning system for high-resolution confocal STEM. *J Electron Microsc.* **57**: 123-127.

## **Chapter 3 Improvement of stage-scanning electron holography**

### **3.1 Introduction**

The technique of stage-scanning electron holography was presented in chapter 2. This technique can provide an interferogram, that is a cosine image of phase, by moving the specimen and recording line intensities in the hologram at different object positions. The resultant interferogram that provides the phase distribution under phase object approximation. This technique can deal with phase object well, because the amplitude of electron wave passed through the specimen can be assumed as 1. However, in practice, for most of the materials, when the electron wave transfers through a specimen, due to the interactions between the electrons and the sample, the amplitude changes because the electrons are absorbed. In such cases, the reconstruction procedure described in chapter 2 is not appropriate. In this chapter, this technique was improved and extended to a non-phase object by recording a series of holograms as a 3-dimensional (3D) data cube at different specimen positions. Slicing the 3D data cube at different CCD pixels produces several interferograms. By applying the proposed reconstruction procedure to these interferograms the phase distribution can be reconstructed with high precision. This technique is expected to overcome the limitation of spatial resolution due to the fringe spacing. The resolution enhancement was demonstrated by observing Co nanoparticles with the stage-scanning electron holography. The results show a better performance than that from the conventional holography based on the Fourier transformation method.

## 3.2 Improvement of stage-scanning electron holography for a non-phase object

### 3.2.1 Principle

The optical configuration in this improved stage-scanning electron holography is the same with the technique presented above, which has been shown in Fig. 2.1. A collimated electron beam illuminates the specimen which is positioned to cover half the field of view. An interference pattern or a hologram is produced by the application of voltage to the biprism located below the specimen with the reference wave and the object wave. The specimen can be moved by the stage-scanning system [1-3].

When the biprism is aligned to the  $y$  direction, the hologram is formed as a result of the interference between the object wave  $\Phi_o$  and the reference wave  $\Phi_r$ , which are given by

$$\Phi_o(n, x, y) = \phi_0(x - n\Delta x, y) \exp[i\eta(x - n\Delta x, y)], \quad (3.1)$$

$$\Phi_r(x, y) = \exp\left[2\pi i \frac{\alpha}{\lambda} x\right]. \quad (3.2)$$

Here  $x$  and  $y$  are coordinates in the hologram,  $\phi_0$  is amplitude,  $\eta$  is phase,  $\Delta x$  is the scan step width of the specimen movement in the  $x$  direction,  $n$  is the step number,  $\lambda$  is the electron wavelength, and the reference wave is tilted by an angle  $\alpha$  relative to the object wave. The hologram intensity is expressed by

$$I(n, x, y) = |\phi_0(x - n\Delta x, y)|^2 + 1 + 2\phi_0(x - n\Delta x, y) \cos\left[\eta(x - n\Delta x, y) + 2\pi \frac{x}{m}\right], \quad (3.3)$$

here,  $m$  refers to the fringe spacing, which corresponds to  $\frac{\lambda}{\alpha}$ .

For a non-phase object in which the amplitude change is not negligible, the simple procedure described in the Eq. (2.5) is not suitable. In this case, the reconstruction procedure for the phase-shifting holography [4, 5] can be applied with a modification.

In phase-shifting holography, a number of holograms with different initial phases are acquired by slightly changing the angle of the incident electron beam, and thus in each hologram the interference fringes are displaced (phase-shifted) while the

specimen position remains the same. The intensity at a certain point on a hologram will vary sinusoidally with the shift in the interference fringes. The phase and amplitude are then retrieved from the sinusoidal curve fitted to the intensity at each point.

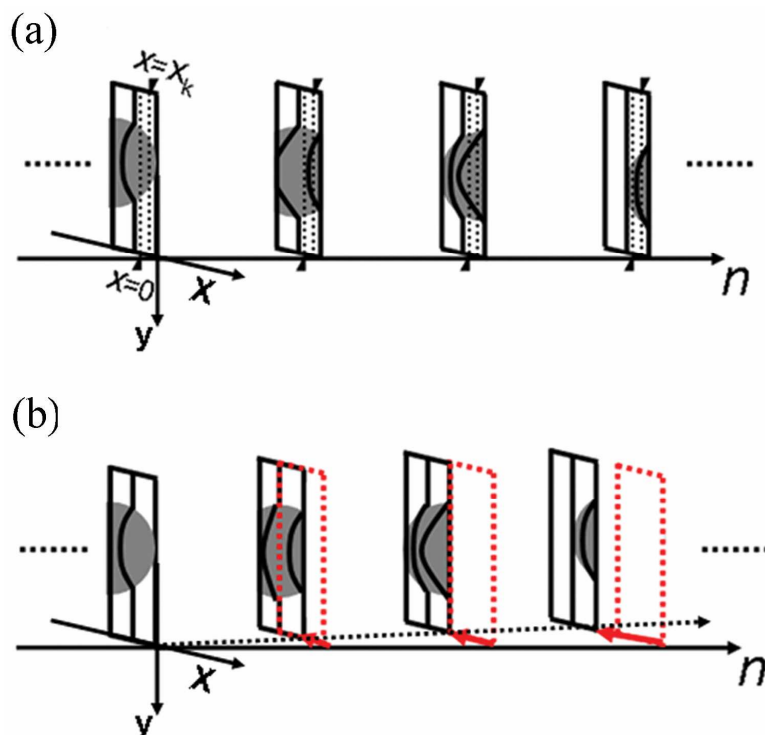


Fig. 3.1 (a) A series of holograms in which only one line intensities at  $x=0$  are captured; (b) aligning the specimen positions in the acquired holograms; the red dotted frames indicate image positions before the alignment.

In this technique, holograms are acquired at each specimen scan step as described by Eq. (3.3), and thus in each hologram the specimen is displaced, while the fringe positions remain the same, as shown in Fig. 3.1(a). Aligning the holograms to compensate for the specimen shift in the  $x$ - $y$  plane (hologram plane) yields a dataset equivalent to the one obtained with the phase-shifting technique. As shown below, at least one fringe spacing of a hologram is sufficient for the reconstruction; therefore, the data array is much smaller in the  $x$  than in the  $y$  direction. After the holograms are aligned in the  $x$ - $y$  plane the overlapped specimen area in the  $x$ -direction becomes small (see Fig. 3.1(b)). Thus, the direct use of phase-shifting holography reconstruction technique is impractical, and a modified reconstruction procedure is

proposed below.

In this procedure, aligning the holograms not in the  $x$ - $y$  plane but in the  $n$ - $y$  plane is performed. A series of 2-dimensional (2D) holograms with different specimen positions can be viewed as a 3D data cube with the dimensions  $(x, y, \Delta x \cdot n)$ . Slicing this cube in the  $(y, \Delta x \cdot n)$  plane at  $x = x_k$  extracts an interferogram as follows

$$\Pi_k(n, y) = |\phi_0(x_k - n\Delta x, y)|^2 + 1 + 2\phi_0(x_k - n\Delta x, y) \cos \left[ \eta(x_k - n\Delta x, y) + 2\pi \frac{x_k}{m} \right]. \quad (3.4)$$

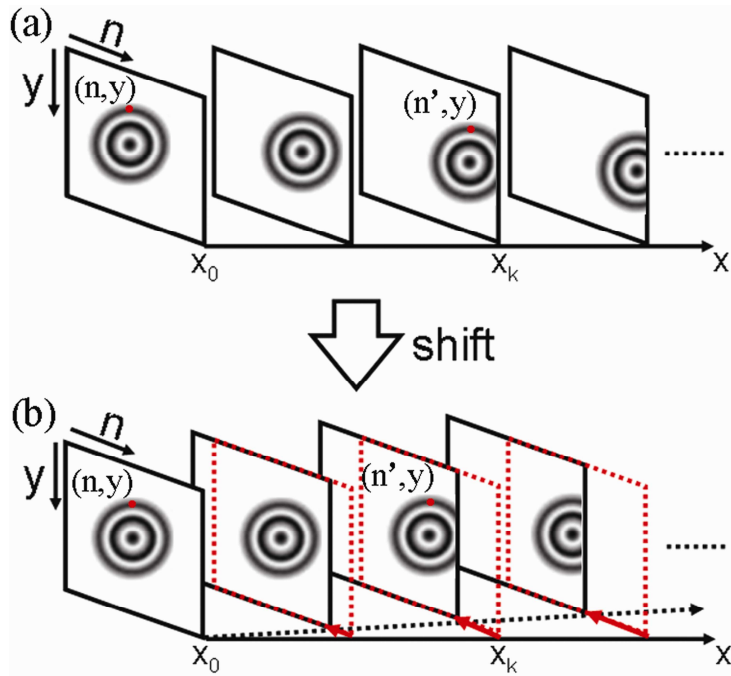


Fig. 3.2 (a) Images obtained by slicing the 3D data cube at different  $x_k$  positions; (b) they are aligned by shifting each slice along the arrows. The red dotted frames indicate image positions before the alignment.

The fringe spacing  $m$  was set to be an integer and a multiple of CCD pixel size in this chapter. Thus  $x_k$  can be expressed as  $x_k = \frac{m}{N}k$ , where  $N$  is the number of divisions of one fringe spacing and  $k = 0, 1, 2, \dots, N-1$ . The specimen position differs for each slice  $x_k$ , as shown in Fig. 3.2(a). In this reconstruction procedure,

the first step is aligning the interferograms in the  $(y, \Delta x \cdot n)$  plane by shifting them in the  $n$ - $y$  plane rather than  $x$ - $y$  plane, so that the specimen position remains the same in the  $(y, \Delta x \cdot n)$  plane. The same specimen points  $(n, y)$  on slice  $x_0$  and  $(n', y)$  on slice  $x_k$  are related as

$$n' = n + \frac{m}{N\Delta x} k. \quad (3.5)$$

After the slice  $x_k$  is shifted by  $\frac{m}{N\Delta x} k$  pixels in the direction  $n$ , as indicated by the arrows in Fig. 3.2(b), the specimen positions of these two slices overlap when viewed along the direction  $x$ . Each new shifted image  $\Pi'_k(n, y)$  (the interferogram in red frame) is defined as

$$\begin{aligned} \Pi'_k(n, y) &= \Pi_k\left(n + \frac{m}{N\Delta x} k, y\right) \\ &= |\phi_0(-n\Delta x, y)|^2 + 1 + 2\phi_0(-n\Delta x, y) \cos\left[\eta(-n\Delta x, y) + 2\pi \frac{k}{N}\right]. \end{aligned} \quad (3.6)$$

Contrary to the phase-shifting technique, since the electron optics is fixed, there is no initial phase term in this expression; instead, the phase difference  $2\pi \frac{k}{N}$  appears in the  $x_k$  slice. Note that since the data cube is sliced at different  $x_k$ , the carrier fringe is absent in Eq. (3.6).

After this alignment, the reconstruction procedure is similar to that of phase-shifting holography. Multiplying by  $\exp\left(-2\pi i \frac{k}{N}\right)$ , and summing both sides

of the Eq. (3.6) over  $k$  yields

$$\begin{aligned} \sum_{k=0}^{N-1} \Pi'_k(n, y) \exp\left(-2\pi i \frac{k}{N}\right) &= N\phi_0(-n\Delta x, y) \cos[\eta(-n\Delta x, y)] \\ &+ iN\phi_0(-n\Delta x, y) \sin[\eta(-n\Delta x, y)] \end{aligned} \quad (3.7)$$

Here, we define

$$C = \sum_{k=0}^{N-1} \Pi'_k(n, y) \cos\left(-2\pi \frac{k}{N}\right) = N\phi_0(-n\Delta x, y) \cos[\eta(-n\Delta x, y)], \quad (3.8)$$

$$S = \sum_{k=0}^{N-1} \Pi'_k(n, y) \sin\left(-2\pi \frac{k}{N}\right) = N\phi_0(-n\Delta x, y) \sin[\eta(-n\Delta x, y)]. \quad (3.9)$$

Then, the phase image and amplitude image can be obtained, respectively, as

$$\eta(-n\Delta x, y) = \tan^{-1}\left(\frac{S}{C}\right), \quad (3.10)$$

$$\phi_0(-n\Delta x, y) = \frac{1}{N} \sqrt{C^2 + S^2}. \quad (3.11)$$

Consider that in the proposed reconstruction procedure, a total of  $N_I$  2D holograms of  $N_2 \times N_3$  size are recorded. Here,  $N_I$  is the number of steps;  $N_2$  and  $N_3$  are the number of pixels within one fringe along the  $y$  and  $x$  direction, respectively. Retrieval of the phase image requires  $N_1 \times N_2 \times N_3$  operations for shifting the interferograms and another  $N_1 \times N_2 \times N_3$  operations for calculating the phase. Because the data size in the  $x$  direction can be small in our reconstruction procedure,  $N_3$  can be much smaller than  $N_I$ .

The phase-shifting technique requires  $N_1 \times N_2 \times N_3$  operations, where  $N_I$  is the number of beam tilts (phase shifts). Let us compare it with the Fourier transformation method for a  $N_2 \times N_3$  hologram. The number of calculations is  $(N_2 \times N_3) \log_2(N_2 \times N_3)$  for Fourier transformation by fast Fourier transform (FFT) and  $(N_2 \times N_3) \log_2(N_2 \times N_3)$  for the inverse transformation. Thus if  $N_2 \times N_3$  is large then the total amount of calculation is much smaller for the Fourier transformation method than for the phase-shifting method or our proposed method. However, the quality of the result in terms of resolution and precision is different, so that direct comparison is difficult.

The phase and amplitude are retrieved in the  $n$ - $y$  plane; thus, the spatial resolution in the  $x$  direction is determined either by the scan step width  $\Delta x$ , the CCD pixel size divided by magnification, or the microscope resolution. In the  $y$  direction, the spatial resolution is determined by the CCD pixel size or microscope resolution. As the reconstruction is possible with one fringe spacing, the above procedure can be performed with a CCD having only a few pixels in the direction  $x$ , which is the direction perpendicular to the biprism wire.

### 3.2.2 Experimental methods

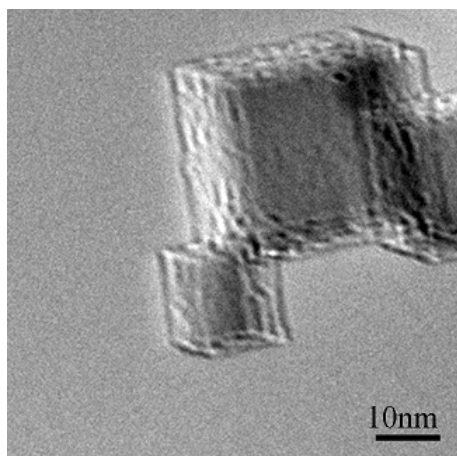


Fig.3.3 TEM image of the MgO crystals.

Experiments were carried out by a JEOL JEM-ARM200F microscope equipped with a biprism. MgO crystals were chosen as the specimen to take stage-scanning electron holography. A MgO crystal (Fig.3.3) of about 15 nm in size attached to a large MgO crystal was chosen as a specimen, and a 3D data cube of holograms with the fringe spacing as 1.1 nm was recorded. The scan step width and the total number of scan steps were 0.11 nm and 200, respectively. In this case, the scan step width was equal to the CCD pixel size. The total acquisition time was about 3 min. 30 s including data transfer time and 1 second exposure time for each scan step.

In order to demonstrate that the proposed reconstruction procedure can determine the object wave independently of the fringe spacing, another 3D data cube was recorded with the same MgO crystal but with wider fringe spacing as 2.2 nm.

### 3.2.3 Results and discussion

Two holograms extracted from the 3D data cube at different specimen positions are shown in Figs. 3.4(a) and (b) as examples. A fringe spacing of 1.1 nm and 10 pixels of the CCD was used for reconstruction. Fig. 3.4(c) shows the phase image retrieved using the proposed reconstruction procedure. The phase changes along the  $x$  direction

in the vacuum region in Fig.3.4 (c) may originate from the charge up of the MgO crystal, but it could also be an artifact which originates from a drift of the biprism, which is difficult to avoid in practice. Thus the line profiles of the net phase shift along the horizontal direction indicated in Figs. 3.4(c) were calculated by subtracting the reference profiles, taken across vacuum regions (lines c2), from the profiles crossing the specimen (lines c1). The resulting profiles are shown in Fig. 3.5. Phase shifts were also measured by a conventional Fourier transformation method with the same fringe spacing of 1.1 nm. The hologram and reconstructed phase image are shown in Fig. 3.6. The profile of phase shift across the MgO crystal indicated in Fig. 3.6 (b) is also added in Fig.3.5 (the red line).

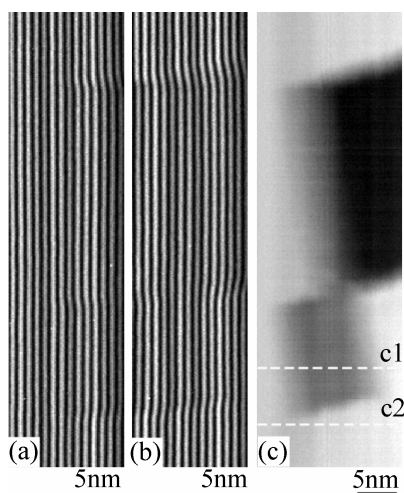


Fig.3.4 (a) and (b) Holograms corresponding to different positions of the MgO crystals; (c) the phase image obtained with the reconstruction procedure for a non-phase object.

By analyzing the profiles in Fig. 3.5, the phase shifts between the uniform thickness area of the specimen and vacuum were calculated as 1.54 and 1.57 radians from the reconstruction procedure with the fringe spacing of 1.1nm (black line), and conventional holography (red line) with the fringe spacing of 1.1nm, respectively. The phase values and profiles obtained by the reconstructions coincide well, demonstrating the validity of this method.

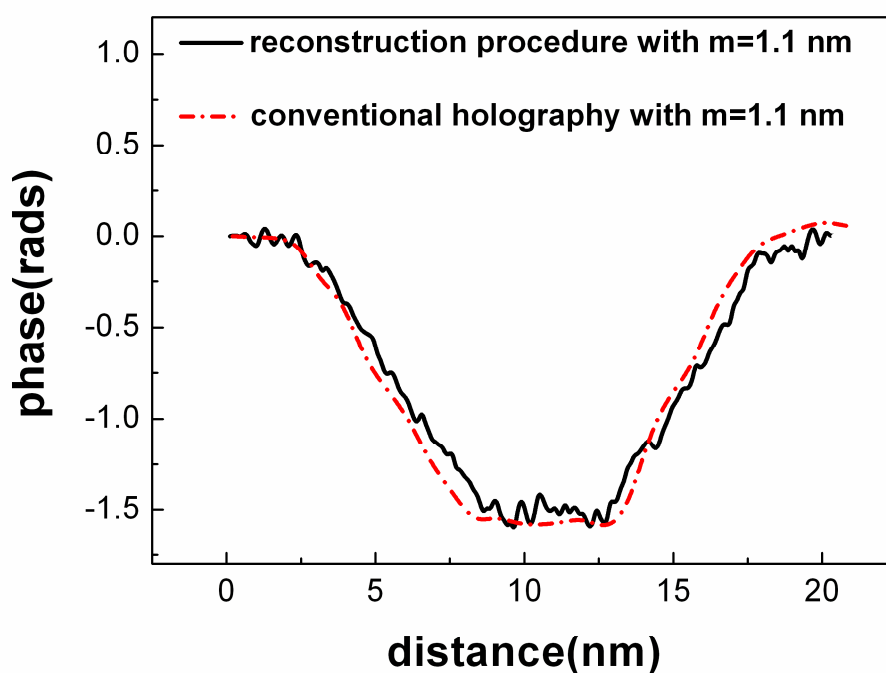


Fig.3.5. Line profiles of the measured net phase shift across the MgO crystal using the reconstruction procedure with the fringe spacing  $m=1.1$  nm, and the conventional holography with the fringe spacing  $m=1.1$  nm. The net phase shift was measured along the horizontal (c1) direction indicated in Figs. 3.4(c).

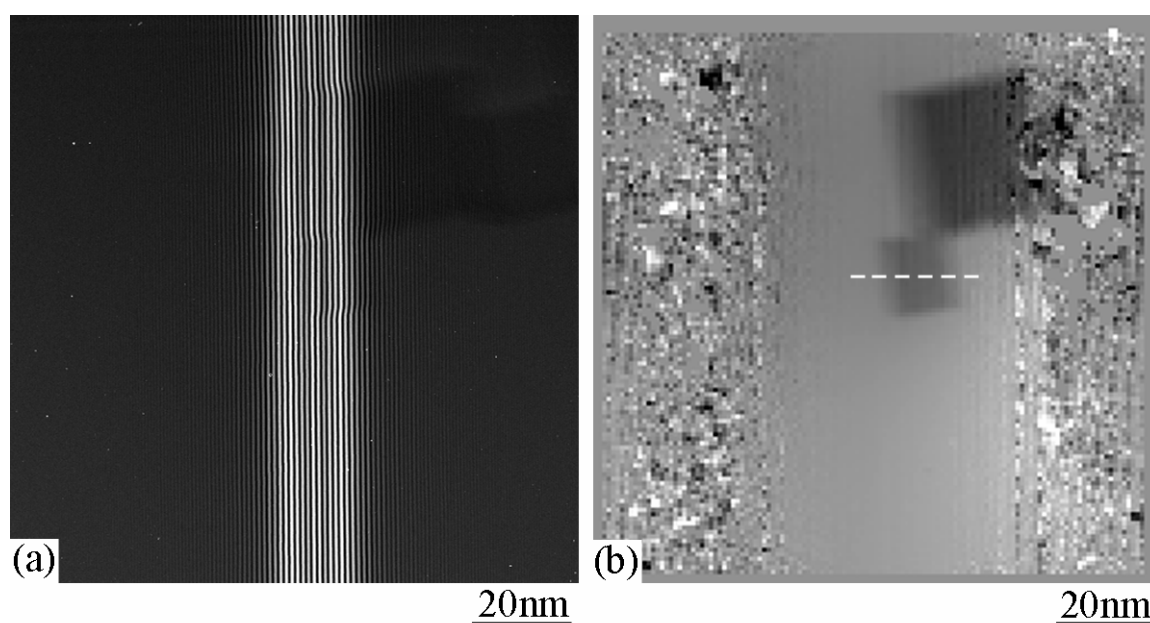


Fig.3.6 (a) Hologram of the MgO crystals using conventional Fourier transformation method; (b) the reconstructed phase image.

It is claimed that in the proposed technique the spatial resolution is not limited by the fringe spacing. That means holograms with coarse fringes can be reconstructed. As is known, in conventional electron holography, after the hologram is Fourier transformed, its selected sideband is inversely Fourier transformed. To avoid any overlap of the Fourier transformation spectra, the distance between the sideband and the center band  $\frac{1}{m}$  controlled by the fringe spacing  $m$  has to be sufficiently large. Thus, the larger is  $m$ , the smaller sideband size should be selected. In the present technique, the phase and amplitude reconstruction is performed in real space, thus the resolution should be irrelevant to the fringe spacing used, as in the phase shifting technique [4, 5], avoiding the need for fine hologram fringes. To demonstrate this point, another 3D data cube using the same MgO crystal was recorded and the same scanning step as in Fig. 3.4, but with a wider fringe spacing (2.2 nm and 20 CCD pixels). The extracted holograms and the phase image from the reconstruction procedure are shown in Fig. 3.7. The fringe spacing used for reconstruction is indicated between the two red lines in Fig. 3.7 (a). The line profile of the net phase shift along horizontal direction (indicated in Fig. 3.7 (c)) were calculated by subtracting the reference profiles taken across the vacuum (line c2) from the profiles taken across the specimen (line c1). The resultant profile is plotted in Fig. 3.8, which corresponds well with the ones obtained from the reconstruction procedure with the fringe spacing of 1.1nm and the conventional Fourier transformation method with the fringe spacing of 1.1nm. This demonstrates the technique can deal well with holograms with coarse fringes.

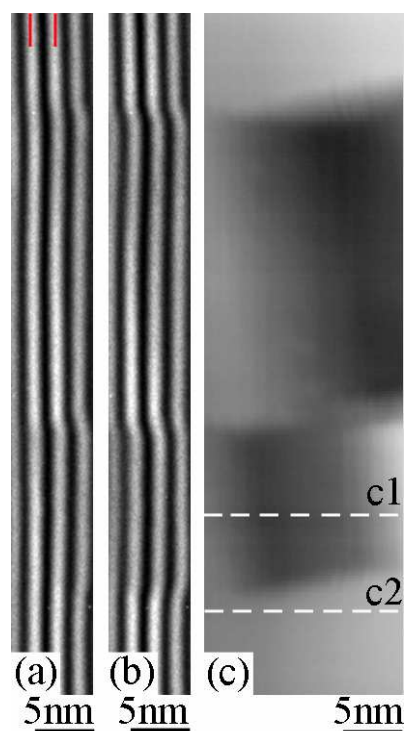


Fig.3.7 (a) and (b) Holograms corresponding to different positions of the MgO crystals with wider fringe spacing ( $m=2.2$  nm), the reconstruction procedure was applied to the fringe spacing between the two red lines indicated in (a); (c) the phase image obtained from the reconstruction procedure for a non-phase object.

The spatial resolution of images reconstructed with the reconstruction procedure depends not on the fringe spacing but on the scan step, the CCD pixel size divided by magnification and the microscope resolution. Another advantage is the potential application for in situ observations of phase distributions, as the phase can be directly extracted from an interferogram by a single scan of the specimen under phase object approximation. Currently, however, the total data acquisition time of this technique depends on the exposure time and the number of scan steps, and the total time needed in the proposed experiments was actually longer than that in the conventional technique due to the long exposure time for each scan step. Therefore, reducing the exposure time but achieving an available signal to noise ratio of holograms should be an important research topic in the future.

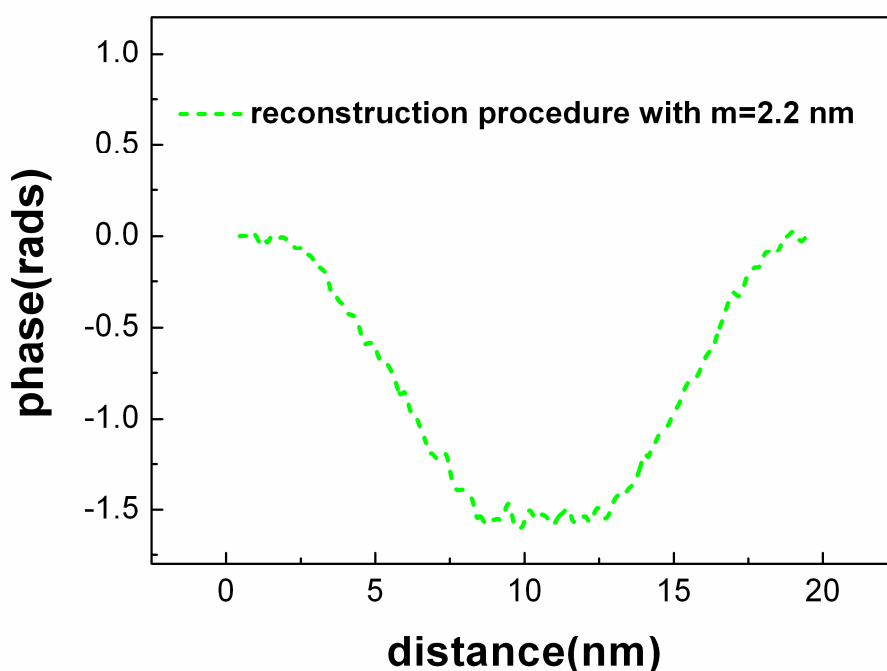


Fig. 3.8 Line profile of the net phase shift calculated by the reconstruction procedure with the fringe spacing  $m=2.2$  nm along the horizontal direction (c1) in Fig.3.7(c).

In real experiments, the drift of the biprism appears as phase change and it is difficult to avoid or distinguish from the field of the specimen or stray fields that come from several different origins. In the case of the stray fields which move along the specimen motion, for example, the electric charge in the specimen, this field affects the phase measurement but this effect is the same as those in the other holography methods. The change of the field due to the relative distance changes between the moving parts of the stage and other fixed parts may causes the artifact which is the type of artifact that unique to the current method. The leakage of the electric field applied across the piezo actuator may also be an origin. In the current experiment any prominent indication of those types of artifact were not observed, and those effects are reasonably small. In other types of stray fields which are not changed with the specimen motion, for example, residual magnetic field from the objective lens, this field does not affect the phase measurement in the reconstruction technique because only the difference from the field at the initial specimen position was used.

### 3.2.4 Drift effect of the biprism and specimen stage and considerations for recording

Several factors should be considered when recording holograms. Since our technique is based on moving the specimen stage to record a series of holograms, special attention should be paid to the drift of the stage perpendicular to the scanning direction. Such drift will hinder alignment of sliced images, resulting in an elongated specimen shape and introducing phase errors. Another experimental factor is biprism drift, which results in intensity shifts and phase shift as mentioned above. This effect can be reduced by stabilizing the prism and by subtracting the background using the vacuum area, provided the electric and magnetic field gradients are neglected.

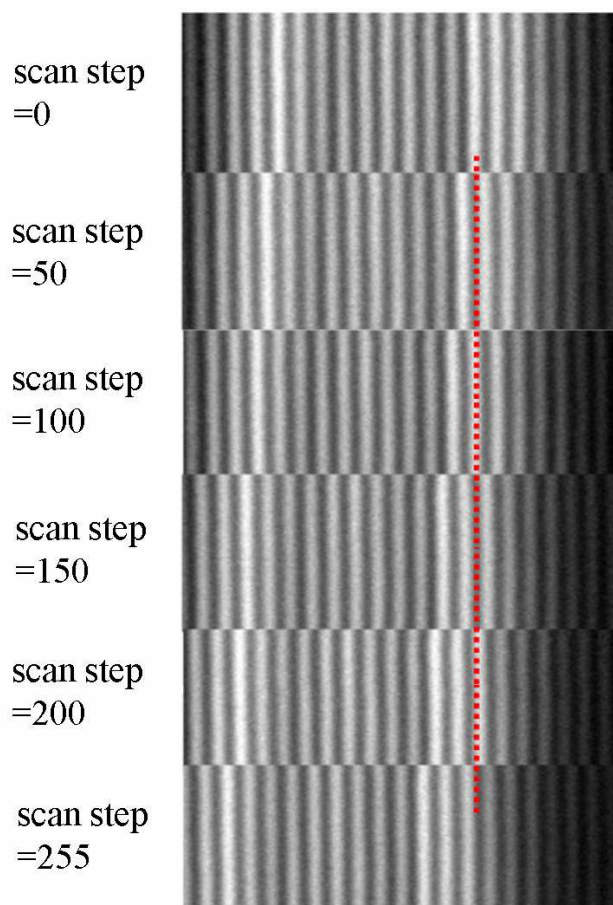


Fig. 3.9 Fringe drifts during the stage-scanning.

The biprism drift causes fringe drift and introduces phase errors in the reconstructed phase image. Fig. 3.9 shows an example of the fringe drift. For example,

the dotted line in Fig. 3.9 is marked a fixed position on the holograms. When the scan step was 0, the dotted line indicated a bright fringe. When the scan step was 255, the bright fringe shifted to another position on the left side of the dotted line. In this case, the fringe shifted about 46 pixels from the beginning of the stage scan to the end. The fringe spacing was about 20 pixels averaged, that means the phase change corresponds to the fringe drift is about 14.4 radians. This phase change presents as the background phase along the horizontal direction in reconstructed phase image. For example, a reconstructed phase image according to our principle using the series of holograms contained biprism drifts is shown in Fig.3.10. Because analyzing the phase change in the vacuum area will show us the influence of the fringe shift. Fig. 3.10 (a) shows the reconstructed phase image of this vacuum area. The profile along the line indicated in Fig.3.10 (a) shows the background phase across vacuum area, which is about 14.2 radians (Fig.3.10 (b)). This value is almost in accordance with the one calculated by measuring the fringe shifts.

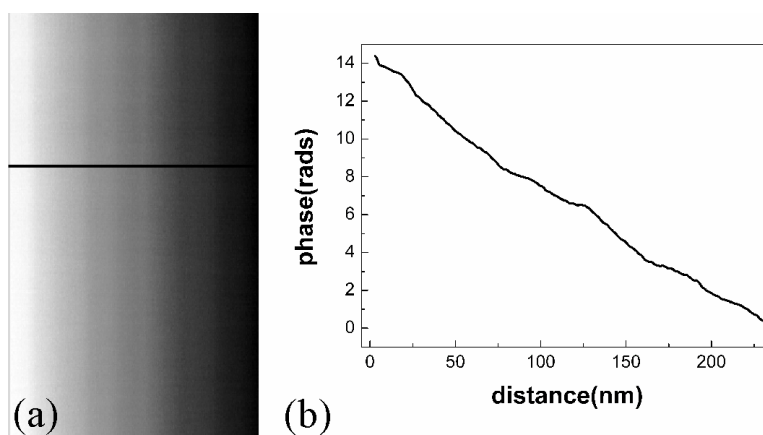


Fig.3.10 (a) shows the reconstructed phase image of a vacuum area; (b) the line profile indicated by the line in (a) shows the background phase across vacuum area.

If the drift speed is constant (in most cases, the drift speed of the biprism can be assumed as a constant), after one scan step is moved, phase change caused by drift is defined as  $\eta_d$ . Then, the intensity distribution of the hologram is written as

$$\begin{aligned}
 & I(n, x, y) \\
 &= \left| \phi_0(x + n\Delta x, y) \right|^2 + 1 + 2\phi_0(x + n\Delta x, y) \cos \left[ \eta(x + n\Delta x, y) + 2\pi \frac{x}{m} + n\eta_d \right]. \quad (3.12)
 \end{aligned}$$

Slicing the recorded data cube at  $x_k$  yields an interferogram

$$\begin{aligned}
 & \Pi_k(n, y) \\
 &= \left| \phi_0(x_k - n\Delta x, y) \right|^2 + 1 + 2\phi_0(x_k - n\Delta x, y) \cos \left( \eta(x_k - n\Delta x, y) + 2\pi \frac{x_k}{m} + n\eta_d \right). \quad (3.13)
 \end{aligned}$$

In order to overlap the specimen positions, a procedure of shifting the specimen position is needed under the relation expressed in Eq. 3.5. The shifted interferogram is expressed by

$$\begin{aligned}
 & \Pi'_k(n, y) = \Pi_k \left( \left( n + \frac{m}{N\Delta x} k \right), y \right) \\
 &= \left| \phi_0 \left( x_k - \left( n + \frac{m}{N\Delta x} k \right) \Delta x, y \right) \right|^2 + 1 \\
 &+ 2\phi_0 \left( x_k - \left( n + \frac{m}{N\Delta x} k \right) \Delta x, y \right) \cos \left( \eta \left( x_k - \left( n + \frac{m}{N\Delta x} k \right) \Delta x, y \right) + 2\pi \frac{x_k}{m} + \left( n + \frac{m}{N\Delta x} k \right) \eta_d \right) \quad (3.14)
 \end{aligned}$$

For convenience, Eq. 3.14 is written in complex form

$$\begin{aligned}
 & \Pi'_k(n, y) \\
 &= C_1 + C_2 \exp \left( i 2\pi \frac{k}{N} \right) \exp \left( i \frac{m}{N\Delta x} \cdot k \cdot \eta_d \right) + C_3 \exp \left( -i 2\pi \frac{k}{N} \right) \exp \left( -i \frac{m}{N\Delta x} \cdot k \cdot \eta_d \right), \quad (3.15)
 \end{aligned}$$

here, we assume

$$C_1 = \left| \phi_0(-n\Delta x, y) \right|^2 + 1;$$

$$C_2 = \phi_0(-n\Delta x, y) \exp[i\eta(-n\Delta x, y) + in\eta_d];$$

$$C_3 = \phi_0(-n\Delta x, y) \exp[-i\eta(-n\Delta x, y) - in\eta_d];$$

Multiplying both sides of equation (3.15) by  $\exp\left(-2\pi i \frac{k}{N}\right)$ , and  $\exp\left(2\pi i \frac{k}{N}\right)$

alternatively, the equation leads to

$$\begin{aligned} & \sum_0^{N-1} \Pi'_k(n, y) \exp\left(-2\pi i \frac{k}{N}\right) \\ &= C_2 \sum_0^{N-1} \exp\left(i \frac{m}{N\Delta x} \cdot k \cdot \eta_d\right) + C_3 \sum_0^{N-1} \exp\left(-i2\pi \frac{k}{N} \times 2\right) \exp\left(-i \frac{m}{N\Delta x} \cdot k \cdot \eta_d\right) \end{aligned} \quad (3.16a)$$

$$\begin{aligned} & \sum_0^{N-1} \Pi'_k(n, y) \exp\left(2\pi i \frac{k}{N}\right) \\ &= C_2 \sum_0^{N-1} \exp\left(i2\pi \frac{k}{N} \times 2\right) \exp\left(i \frac{m}{N\Delta x} \cdot k \cdot \eta_d\right) + C_3 \sum_0^{N-1} \exp\left(-i \frac{m}{N\Delta x} \cdot k \cdot \eta_d\right) \end{aligned} \quad (3.16b)$$

Next, we define

$$C'_2 = a + bi,$$

$$C'_3 = a - bi,$$

and equation (3.16.a) and (3.16.b) can be expressed by

$$A = (a + bi)B + (a - bi)C, \quad (3.17a)$$

$$D = (a + bi)E + (a - bi)F, \quad (3.17b)$$

where

$$A = \sum_0^{N-1} \Pi'_k(n, y) \exp\left(-2\pi i \frac{k}{N}\right);$$

$$B = \sum_0^{N-1} \exp\left(i \frac{m}{N\Delta x} \cdot k \cdot \eta_d\right);$$

$$C = \sum_0^{N-1} \exp\left(-2\pi i \frac{k}{N} \times 2\right) \exp\left(-i \frac{m}{N\Delta x} \cdot k \cdot \eta_d\right);$$

$$D = \sum_0^{N-1} \Pi'_k(n, y) \exp\left(2\pi i \frac{k}{N}\right);$$

$$E = \sum_0^{N-1} \exp\left(2\pi i \frac{k}{N} \times 2\right) \exp\left(i \frac{m}{N\Delta x} \cdot k \cdot \eta_d\right);$$

$$F = \sum_0^{N-1} \exp\left(-i \frac{m}{N\Delta x} \cdot k \cdot \eta_d\right).$$

Here, we use these valuables  $A$ ,  $B$ ,  $C$ ,  $D$ ,  $E$ ,  $F$  to express the relative terms in Eqs.(3.16 a) and (3.16 b) for simplicity. It is easy to calculate  $B$ ,  $C$ ,  $E$  and  $F$  with

$\eta_d$  which can be known by measuring the total phase change caused by fringe drift.

$A$  and  $D$  can be obtained from the summation of series shifted images. Then we can calculate

$$a = \frac{A(E - F) - D(B - C)}{2(CE - BF)}, \quad (3.18a)$$

$$b = \frac{A(E + F) - D(B + C)}{2(BF - CE)}, \quad (3.18b)$$

and retrieval to  $C'_2$  and  $C'_3$ . Corrected phase and amplitude images are reconstructed by

$$\eta_{corr}(-n\Delta x, y) = \tan^{-1}\left(\frac{\text{Im}(C'_2)}{\text{Re}(C'_2)}\right) - n\eta_d, \quad (3.19a)$$

and

$$\phi_{0corr}(-n\Delta x, y) = \sqrt{C'_2 \times C'_3}. \quad (3.19b)$$

The term  $n\eta_d$  in equation (3.17.a) is a slope ratio, meaning  $\eta_{corr}(-n\Delta x, y)$  lying on the phase slope of  $n\eta_d$  due to the fringe drift, which results in the background phase change of vacuum area.

### 3.3 Demonstration of resolution improvement in stage-scanning electron holography

#### 3.3.1 Experimental methods

The major difference between the stage-scanning electron holography and conventional holography based on the Fourier transformation is the necessity of fine fringe spacing. In the conventional technique, the fringe spacing should be about three times finer than the desired spatial resolution [7-14]. However, in the proposed stage-scanning electron holography technique is that the spatial resolution of the reconstructed phase image is determined not by the interference fringe spacing, but by

the scan step and by the microscope resolution or the pixel size along the  $y$  direction. This is the principal difference from the conventional holography. Because the Fourier transformation method is unnecessary to reconstruct the phase, coarse fringes with high contrast can be used, which would also be helpful for improving the precision of the reconstructed phase image.

In the session, an experiment was designed by observation Co nano-particles in a low-magnification mode in which the objective lens of the microscope is switched off. To realize the electron holography configuration the first intermediate lens is also turned off, which limits the choice of magnification. Therefore it may be difficult to have an appropriate combination of magnification and fringe spacing for performing conventional electron holography on specimens with micrometer-scale features. The stage-scanning electron holography technique should solve this problem by overcoming the limitation between the spatial resolution and fringe spacing. This flexibility is especially important for observing magnetic specimens, which must be located in a low-field region to avoid unwanted magnetic saturation.

Experiments were carried out in the low-magnification mode with a JEOL JEM-ARM200F microscope (200 kV) equipped with a biprism and a stage-scanning system. Co nanoparticles with a diameter of 10-20 nm deposited on a carbon film were used as a sample.

Figure 3.11 shows a bright-field TEM image of Co particles dispersed on the edge of a carbon film. Holograms were acquired at different specimen positions, by moving the specimen with the stage-scanning system, and saved as a 3D data cube with dimensions of 155 pixels $\times$ 260 pixels $\times$ 90 steps. The total acquisition time was about 1 min 40 s, including data transfer and 1 second exposure for each scan step.

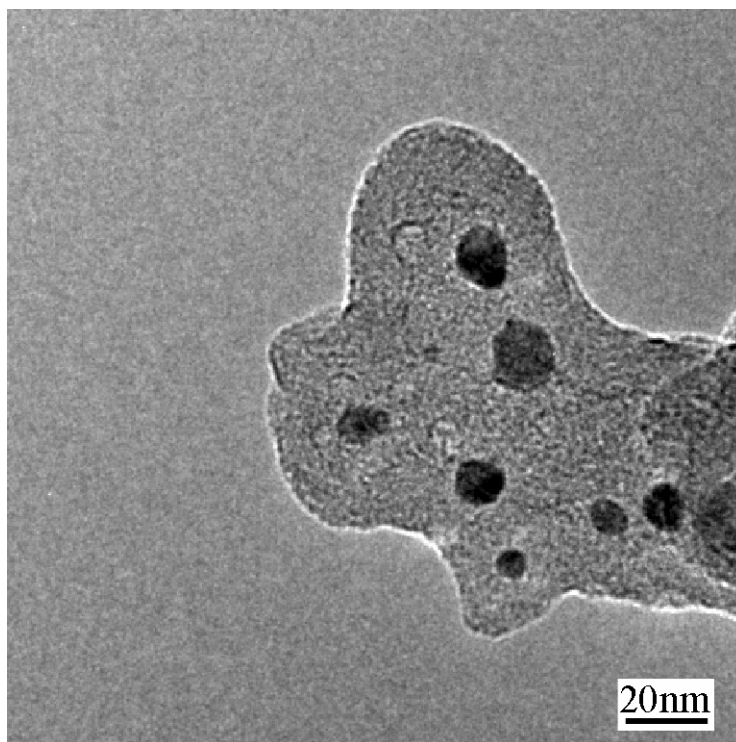


Fig. 3.11 TEM image of Co particles.

### 3.3.2 Results and discussion

Two holograms, recorded at different specimen positions and extracted from the 3D data cube, are shown in Figs. 3.12 (a) and (b). In this case the fringe spacing was 26 nm or 10 pixels, which is wider than the diameter of the particles. In the extracted holograms (a) and (b), the particles cannot be distinguished but only the fringe shift on the specimen can be seen. The phase distribution of the particles (Fig. 3.12 (c)) was reconstructed using 10 lines of CCD pixels as a fringe, 90 holograms, and stage-scanning distance of 230 nm. The Co particles are well distinguished in Fig. 3.12 (c). Figure 3.13 shows the line profile across a Co particle indicated by the white line in Fig. 3.12(c). The profile shows the shape of the particle with a phase change of about 1.2 radians and a diameter of about 15.5 nm, which is close to 14.1 nm measured from the TEM image of Fig. 3.11.

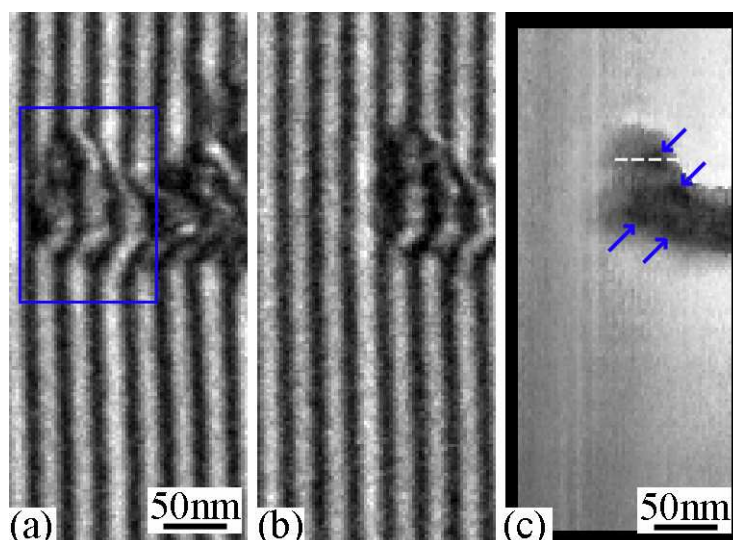


Fig. 3.12 Two extracted holograms of the Co particles (a) and (b) with a fringe spacing of 26 nm; The specimen moved from the position in hologram (a) to the position in hologram (b) due to the movement of the specimen stage; (c) The phase image obtained with the stage-scanning technique.

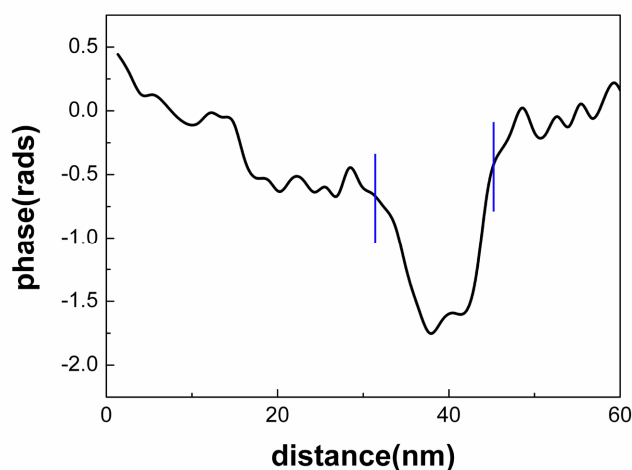


Fig. 3.13 Profile of phase change of the Co particle indicated by the white line in Fig. 3 (c).

For comparison, the same Co particles were observed with the conventional holography technique based on the Fourier transformation method. In this case fine fringe spacing was necessary to attain a high resolution. Otherwise, windowing the sideband in the Fourier space might induce artifacts in the real space [7]. Therefore, a fringe spacing of 17 nm was used in the same optical configuration with a higher biprism voltage, which was the finest fringe spacing considering the fringe contrast

and signal-to-noise ratio of the holograms given the limited freedom of magnification in this experiment. Figures 3.14(a) and (b) show the hologram and the phase distribution of the Co particles retrieved via Fourier transformation, respectively. It is difficult to distinguish the phase of each Co particle in this reconstructed phase image. Comparing the results from these two techniques, the stage-scanning holography yields higher resolution with a wider fringe spacing than the conventional holography based on the Fourier transformation method. The former technique is useful when fine fringes cannot be obtained but a high resolution is needed.

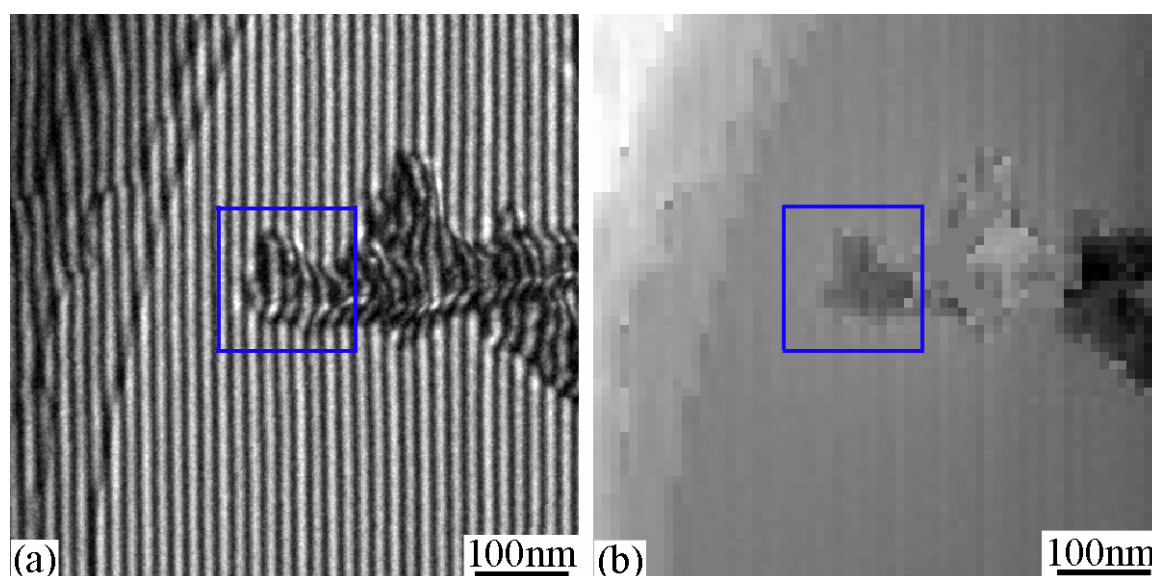


Fig. 3.14 Hologram taken with a fine fringe spacing of 17 nm by conventional electron holography (a) and the reconstructed phase image (b). The area within the blue box is the same area that was observed by the stage-scanning holography.

### 3.4 Conclusions

Based on the stage-scanning electron holography proposed in Chapter 2, an improvement of the technique is presented and extended the usage to non-phase object. This technique yields the phase distribution without the use of Fourier transformation, and therefore the spatial resolution can be determined independently of the fringe spacing in the holograms. Experimental results for MgO crystals demonstrated the practicability and reliability of this technique. The spatial resolution

can be determined independently of the fringe spacing of the holograms by applying the stage-scanning electron holography in a low-magnification mode to Co particles. Higher spatial resolution was achieved compared with that of conventional electron holography based on the Fourier transformation method. The stage-scanning electron holography is thus useful in a low-magnification mode when fine fringes cannot be obtained due to the limited TEM magnification.

## Reference

- [1] Takeguchi M, Shimojo M, Tanaka M, Che R, Zhang W and Furuya K (2006) Electron holographic study of the effect of contact resistance of connected nanowires on resistivity measurement. *Surf Interface Anal.* **38**: 1628-1631.
- [2] Takeguchi M, Hashimoto A, Shimojo M, Mitsuishi K and Furuya K (2008) Development of a stage-scanning system for high-resolution confocal STEM. *J Electron Microsc.* **57**: 123-127.
- [3] M. Takeguchi, K. Mitsuishi, D. Lei and M. Shimojo (2011) Development of sample-scanning electron holography, *Microsc Microanal.* **17**(Suppl 2):1230.
- [4] Q. Ru, J. Endo, T. Tanji and A. Tonomura (1991) Phase-shifting electron holography by beam tilting, *Appl Phys Lett.* **59**: 2372(1991).
- [5] Q. Ru, G. Lai, K. Aoyama, J. Endo and A. Tonomura (1994) Principle and application of phase-shifting electron holography. *Ultramicroscopy.* **55**: 209-220.
- [6] K. Yamamoto, Y. Sugawara, M. R. McCartney and D. J. Smith (2010) Phase-shifting electron holography for atomic image reconstruction. *J. Electron Microsc.* **59**: s81-s88.
- [7] H. Lichte, D. Geiger, A. Harscher, E. Heindl, M. Lehmann, D. Malamidis, A. Orchowski and W. Rau (1996) "Artifacts in electron holography", *Ultramicroscopy*, **64**: 67-77.
- [8] W. J. de Ruijter and J. K. Weiss (1993) Detection limits in quantitative off-axis electron holography, *Ultramicroscopy*, **50**: 269-283.
- [9] K. Yamamoto, T. Hirayama and T. Tanji (2004) Off-axis electron holography without Fresnel fringes, *Ultramicroscopy*, **101**: 265-269.
- [10] H. Lichte (2008) Performance limits of electron holography, *Ultramicroscopy*, **108**(3):256-62.
- [11] M. R. McCartney and D. J. Smith (1994) Direct observation of potential distribution across Si/Si p-n junctions using off-axis electron holography, *Appl. Phys. Lett.* **65**:2603-2605.
- [12] T. Latychevskaia, P. Formanek, C. T. Koch and A. Lubk (2010) Off-axis and

inline electron holography: Experimental comparison, *Ultramicroscopy*, 110: 472-482.

[13] G. Lai, Q. Ru, K. Aoyama and A. Tonomura (1994) Electron-wave phase-shifting interferometry in transmission electron microscopy. *J Appl Phys.* **76**: 39.

[14] K. Harada, A. Tonomura, T. Matsuda, T. Akashi and Y. Togawa (2004) High-resolution observation by double-biprism electron holography. *J Appl Phys.* **96**: 6097.

## **Chapter 4 Super-resolution phase reconstruction technique in stage-scanning electron holography**

### **4.1 Introduction**

Images with high resolution are desired and required in most imaging applications because a high resolution image can offer more details that may be critical in various applications. Since the 1970s, charged-coupled device (CCD) and CMOS image sensors have been widely used to capture digital images. These sensors are suitable for most imaging applications; however, the current resolution level and consumer price will not satisfy the future demand [1].

In optical imaging fields, there are many solutions to increase the spatial resolution. The most direct one is to increase the number of pixel per unit area by sensor manufacturing techniques [1]. However, if the pixel size decreases, the amount of light available also decreases. It therefore generates shot noise that degrades the image quality severely. Another method is increasing the chip size to enhance the spatial resolution. However, this approach is not considered effective because large capacitance makes it difficult to speed up a charge transfer rate. The high cost for high precision optics and image sensors is also an important concern in many commercial applications regarding high resolution imaging. Therefore, a new approach toward increasing spatial resolution is required to overcome these limitations of the sensors and optics manufacturing technology.

One promising approach is to use signal processing techniques to obtain a high resolution image from observed multiple low-resolution images. Recently, such a resolution enhancement approach has been one of the most active research areas, and it is called super resolution (SR) image reconstruction or simply resolution enhancement in the literatures [1-22].

The basic premise for increasing the spatial resolution in SR techniques is the availability of multiple low resolution images captured from the same scene. In SR, typically, the low resolution images show different “looks” at the same scene. This is because the low resolution images are shifted with sub-pixel precision compared with each other [1]. When the low resolution images are shifted by integer units, each image contains the same information of the specimen, and thus there is no new information that can be used to reconstruct a high resolution image. When the low resolution images have different sub-pixel shifts from each other, each image cannot be obtained from the others. In this case, by combining these low resolution images, the new information contained in each low resolution image can be exploited to obtain a high resolution image, SR image reconstruction is possible.

In chapters 2 and 3, a stage-scanning electron holography technique under phase object approximation [23] was proposed and extended to non-phase object. During the stage-scanning, the key parameter is the width of stage movement in a single scan step, in other words, scan step width. This can be categorized into two cases. One is that the scan step width is an integer multiple of the CCD pixel size. In this case, the spatial resolution of the reconstructed phase image is determined by the CCD pixel size divided by magnification, or the microscope resolution. The availability of the stage-scanning holography technique in this integer case has been demonstrated. The other is a non-integer case, the main focus of this chapter. In this case, the holograms are recorded with sub-pixel specimen shifts. Taking line intensities of the recorded holograms can produce different interferograms which contain different phase information due to sub-pixel specimen shifts. These different interferograms result in different phase images. The resultant phase images then can be interlaced to form a new phase image with higher pixel density. The spatial resolution of this new phase image is enhanced than the CCD pixel size divided by the magnification. This is called multiple-frame super resolution technique [26], which is widely used in optical imaging system for utilizing information from a set of low-resolution images with sub-pixel shifts of the specimens to compose a high-resolution image. Several SR reconstruction algorithms have been proposed [27-30]. The super-resolution

reconstruction technique can obtain a high resolution image from observed multiple low-resolution images. In this super-resolution reconstruction technique, the low resolution images are shifted with sub-pixel precision and the motion is irregular in general. By combining these low resolution images, the information contained in each low resolution image can be exploited to obtain a high resolution image, thus super-resolution image reconstruction is possible. However, in this case, the algorithm can be simplified because the specimen can be moved regularly by the stage-scanning system and the specimen motion is easy to estimate. In this chapter, a simplified SR technique is introduced into electron holography, and the principle and an application of this technique is proposed. The super-resolution phase reconstruction technique provides a potential way to improve the spatial resolution compared with the conventional electron holography techniques.

## 4.2 Principle

Figure 1.1 outlines an electron holography setup that employs a stage scanning system [31-33]. When the biprism is aligned to the  $y$  direction, the intensity of electron hologram is expressed by:

$$I(n, x, y) = |\phi_0(x - n\Delta x, y)|^2 + 1 + 2\phi_0(x - n\Delta x, y) \cos \left[ \eta(x - n\Delta x, y) + 2\pi \frac{x}{m} \right]. \quad (4.1)$$

Here  $x$  and  $y$  are coordinates in the hologram,  $\phi_0$  is amplitude,  $\eta$  is phase,  $n$  is the step number,  $m$  refers to the fringe spacing, and  $\Delta x$  is the scan step in the  $x$  direction; the latter can be calculated as  $\frac{\Delta a}{\Delta n}$ , where  $\Delta a$  is the scanned distance and  $\Delta n$  is the number of steps.

Firstly, a series of two-dimensional (2D) holograms at different specimen positions was recorded and stacked into a 3D dataset that is called as a 3D data cube. The value of  $\Delta x$  can be arbitrary or a multiple of the CCD pixel size. To illustrate the specimen shift across CCD pixels, in Figs. 4.1- 4.3 below, each sub-pixel feature of the specimen was described by one letter A to Z, assuming all features are dissimilar.

Each cell corresponds to one pixel and contains five letters. The direction of specimen movement is along the  $x$  axis. Slicing the obtained 3D data cube in the  $(n \cdot \Delta x, y)$  plane at  $x = x_k$  extracts an interferogram as follows:

$$\Pi_k(n, y) = \left| \phi_0(x_k - n\Delta x, y) \right|^2 + 1 + 2\phi_0(x_k - n\Delta x, y) \cos \left[ \eta(x_k - n\Delta x, y) + 2\pi \frac{x_k}{m} \right]. \quad (4.2)$$

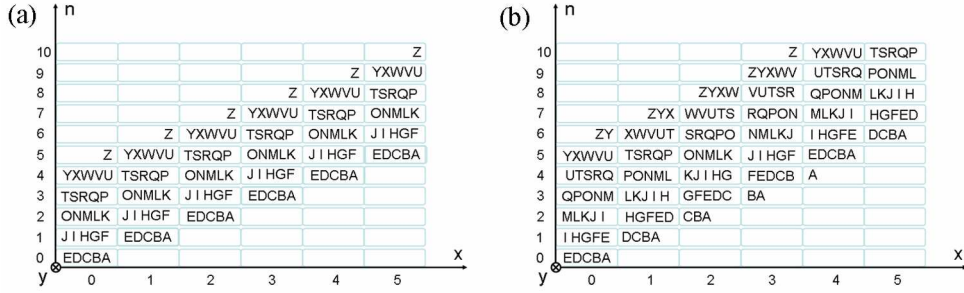


Fig.4.1 Schematic of the recorded 3D data cube with different specimen positions viewed along the  $y$  direction. The scan step width  $\Delta x$  equals to 1 CCD pixel (a) or  $\frac{4}{5}$  CCD pixels (b).

If  $\Delta x$  is a multiple of CCD pixel size, as shown in Fig. 4.1 (a), then all features in any pixel at a given  $x$  are dissimilar. If  $\Delta x$  is arbitrary, as shown in Fig. 4.1 (b), then some pixels at a given  $x$  contain the same specimen feature. In this case, the information contained in each sliced interferogram at  $x = x_k$  can be exploited to obtain an image with a higher resolution compared to the integer-step case. These two cases are elaborated as follows.

#### 4.2.1 Scan step is a multiple of the CCD pixel size

Slicing the 3D data cube in the  $(n \cdot \Delta x, y)$  plane at  $x = x_k$  extracts a sliced interferogram as described by Eq. (4.4). The specimen position differs on each sliced interferogram at  $x_k$ . Then each sliced interferogram is shifted in the  $(n \cdot \Delta x, y)$  plane as follows. If the same specimen point is located at  $(n, y)$  on the sliced interferogram

at  $x = x_0$  and at  $(n', y)$  on the sliced interferogram at  $x = x_k$  then

$$n' = n + \frac{x_k}{\Delta x}. \quad (4.3)$$

Here assuming  $x_0 = 0$  for simplicity. After the sliced interferogram at  $x = x_k$  is shifted by  $\frac{x_k}{\Delta x}$  pixels in the  $n$  direction, the specimen positions on these two sliced interferograms overlap with each other when viewed along the  $x$  direction. Each new shifted interferogram  $\Pi'_k(n, y)$  is defined as

$$\begin{aligned} \Pi'_k(n, y) &= \Pi_k\left(n + \frac{x_k}{\Delta x}, y\right) \\ &= \left| \phi_0(-n\Delta x, y) \right|^2 + 1 + 2\phi_0(-n\Delta x, y) \cos \left[ \eta(-n\Delta x, y) + 2\pi \frac{x_k}{m} \right]. \end{aligned} \quad (4.4)$$

For convenience, Eq. (4.4) can be written in a complex form as

$$\Pi'_k(n, y) = C_1 + C_2 \exp(2\pi i \frac{x_k}{m}) + C_3 \exp(-2\pi i \frac{x_k}{m}), \quad (4.5)$$

where

$$C_1 = \left| \phi_0(-n\Delta x, y) \right|^2 + 1,$$

$$C_2 = \phi_0(-n\Delta x, y) \exp[i\eta(-n\Delta x, y)],$$

$$C_3 = \phi_0(-n\Delta x, y) \exp[-i\eta(-n\Delta x, y)].$$

Multiplying both sides of Eq. (4.5) by  $1$ ,  $\exp\left(-2\pi i \frac{x_k}{m}\right)$  and  $\exp\left(2\pi i \frac{x_k}{m}\right)$ , then summing both sides over  $k$ , the resultant function can be expressed in a matrix form as

$$\begin{pmatrix} N & \sum_0^{N-1} \exp(2\pi i \frac{x_k}{m}) & \sum_0^{N-1} \exp(-2\pi i \frac{x_k}{m}) \\ \sum_0^{N-1} \exp(-2\pi i \frac{x_k}{m}) & N & \sum_0^{N-1} \exp(-4\pi i \frac{x_k}{m}) \\ \sum_0^{N-1} \exp(2\pi i \frac{x_k}{m}) & \sum_0^{N-1} \exp(4\pi i \frac{x_k}{m}) & N \end{pmatrix} \begin{pmatrix} C_1 \\ C_2 \\ C_3 \end{pmatrix} \\
 = \begin{pmatrix} \sum_0^{N-1} \Pi'_k(n, y) \\ \sum_0^{N-1} \Pi'_k(n, y) \exp(-2\pi i \frac{x_k}{m}) \\ \sum_0^{N-1} \Pi'_k(n, y) \exp(2\pi i \frac{x_k}{m}) \end{pmatrix} \quad (4.6)$$

$C_1$ ,  $C_2$  and  $C_3$  can be determined by computing the following matrix function

$$\begin{pmatrix} C_1 \\ C_2 \\ C_3 \end{pmatrix} = \begin{pmatrix} N & \sum_0^{N-1} \exp(2\pi i \frac{x_k}{m}) & \sum_0^{N-1} \exp(-2\pi i \frac{x_k}{m}) \\ \sum_0^{N-1} \exp(-2\pi i \frac{x_k}{m}) & N & \sum_0^{N-1} \exp(-4\pi i \frac{x_k}{m}) \\ \sum_0^{N-1} \exp(2\pi i \frac{x_k}{m}) & \sum_0^{N-1} \exp(4\pi i \frac{x_k}{m}) & N \end{pmatrix}^{-1} \cdot \begin{pmatrix} \sum_0^{N-1} \Pi'_k(n, y) \\ \sum_0^{N-1} \Pi'_k(n, y) \exp(-2\pi i \frac{x_k}{m}) \\ \sum_0^{N-1} \Pi'_k(n, y) \exp(2\pi i \frac{x_k}{m}) \end{pmatrix} \quad (4.7)$$

Then the phase and amplitude images can be obtained as

$$\eta(-n\Delta x, y) = \tan^{-1} \left( \frac{\text{Im}[C_2]}{\text{Re}[C_2]} \right) = \tan^{-1} \left( -\frac{\text{Im}[C_3]}{\text{Re}[C_3]} \right), \quad (4.8)$$

$$\phi_0(-n\Delta x, y) = \sqrt{C_2 \times C_3}, \quad (4.9)$$

where Im and Re denote the imaginary and real parts of the complex value in brackets, respectively.

#### 4.2.2 Arbitrary scan step

Figure 4.1(b) presents an example with an arbitrary scan step ( $\frac{4}{5}$  pixels). Since

the shift of the same specimen point on a sliced interferogram cannot be compensated by the scan before  $n=4$  (as shown in Fig. 4.2(a)), the signal from that point will appear not in the neighboring sliced interferogram, but in another, more remote interferogram. In Fig. 4.2(a), the information in the pixel ( $n=0, x=0$ ) in the sliced interferogram at  $x_k=0$  will appear again in the sliced interferograms at  $x_k=4, 8, 12, etc.$  However, the specimen position differs on each sliced interferogram at  $x_k$ . Then a necessary operation is overlapping the same specimen positions on this series of sliced interferograms using Eq. 4.4.

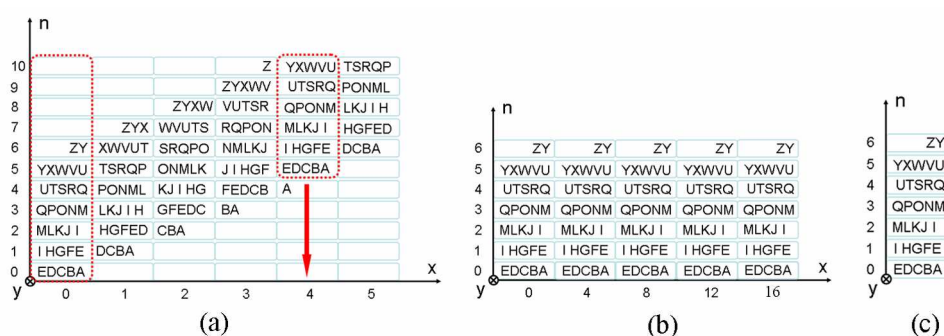


Fig.4.2 (a) Schematic of the procedure to shift the sliced interferograms; (b) the specimen positions on each sliced interferogram are overlapped with each other after the shifting procedure; (c) a phase image reconstructed from the series of sliced interferograms shown in (b).

For instance, in Figs. 4.2 (a) and (b), assuming one fringe spacing has 10 pixels and one scan step width is  $\frac{4}{5}$  pixel, and 2 fringes are selected for reconstruction, which correspond to 20 pixels. Shifting the specimen positions on the series of sliced interferograms at  $x_k=0, 4, 8, 12, 16$  to overlap with each other (Fig. 4.2 (b)). Using the Eq. (8), the phase (Fig. 4.2 (c)) and amplitude images can be obtained from this series of sliced interferograms.

Please note that between the sliced interferograms at  $x_k=0, 4, 8, 12, and 16$  in Fig. 4.2 (a) there are many cells that contain unused information on the specimen, for example, the interferograms at  $(x_k+1)=1, 5, 9, 13 and 17$ . These cells can be

employed for reconstruction, for example, by slicing the data cube at  $x = (x_k + 1)$  and carrying out the reconstruction through shifting the specimen position and multiplying by  $1, \exp\left(-2\pi i \frac{x_k + 1}{m}\right)$ , and  $\exp\left(2\pi i \frac{x_k + 1}{m}\right)$ . Such slicing and reconstruction procedures can be repeated 4 times from  $x_k$  to  $(x_k + 3)$ , yielding four sets of sliced interferograms and phase images, as shown in Fig. 4.3 (a). After shifting the specimen positions on these phase images along the arrows in Fig. 4.3 (a), the specimen features have sub-pixel shifts as shown in Fig. 4.3 (b). As shown in Fig. 4.3 (c), the resultant four low-resolution phase-images can be interlaced to yield an SR phase image that has a 4 times higher pixel density and a higher spatial resolution than its individual components. Note that the specimen does not move relatively to the CCD pixels in conventional electron holography, and thus the super-resolution phase reconstruction is a unique feature of the proposed technique.

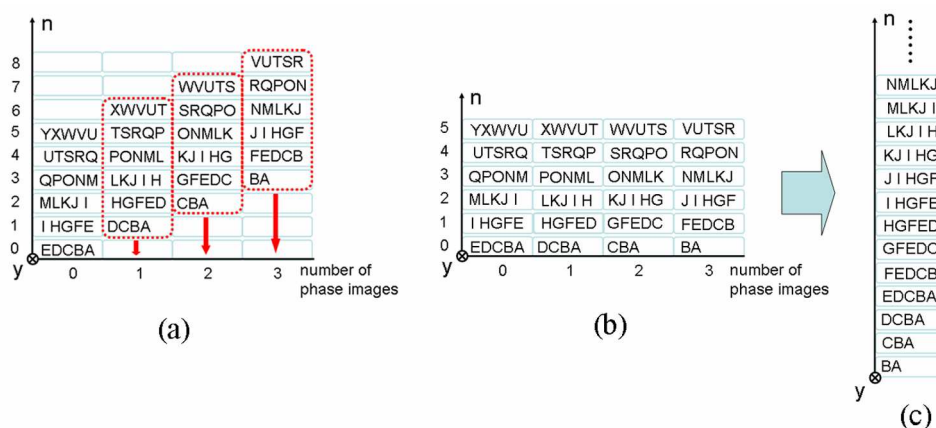


Fig.4.3 (a) Schematic of four phase-images reconstructed from four series of sliced interferograms; (b) the specimen positions on the four phase-images are overlapped by shifting along the arrows in (a); (c) the phase image with a high pixel density obtained by interlacing the four phase-images in (b).

### 4.3 Simulation for super resolution electron holography

A model of specimen having various line-spacing was simulated. This specimen

was a pure phase object with the size of 150 pixels×100 pixels, as shown in Fig. 4.4(a). The profile in Fig.4.4 (c) of this specimen shows the information of this specimen in detail. However, sometimes it is difficult to observe such information in TEM observation due to the insufficient CCD pixels or low microscopy resolution. Thus, a new specimen was reconstructed by re-sampling one pixel from every five pixels along  $x$  direction from the model specimen written above. Fig.4.4 (b) shows the re-sampled specimen with the size of 30 pixels×100 pixels. Fig.4.4 (d) is the line profile indicated by the line in Fig. 4.4 (b), some region cannot be observed in detail compared with the one shown in Fig. 4.4 (c). Using this re-sampled specimen, a 3D data cube was simulated as a series of holograms and recorded with the size of 120 pixels×200 pixels×64 steps and the scan step width was  $\frac{4}{5}$  pixel. Figs. 4.5(a) and (b) show two extracted holograms from the simulated 3D data cube. A phase image can be obtained (Fig.4.5 (c)) by performing the reconstruction procedure using one series of slices according to Fig. 4.2. The line profile in Fig. 4.5(e) shows the phase change of the re-sampled specimen. Due to the lack of pixel density, the resolution of this phase image is not significantly improved and it is hard to tell the intrinsic information as well as the profile shown in Fig.4.4 (c). However, if several series of slices are used for reconstruction as shown in Fig.4.3, 4 different phase images can be obtained in this case. After interlacing these 4 phase images according to Fig. 4.3(c), an interlaced phase image can be obtained (Fig.4.5 (d)). Then the line profile of the interlaced phase image is shown in Fig. 4.5 (f). The resolution of this phase image is highly improved, and it is easy to determine the intrinsic information as well as the original specimen from this interlaced phase image.

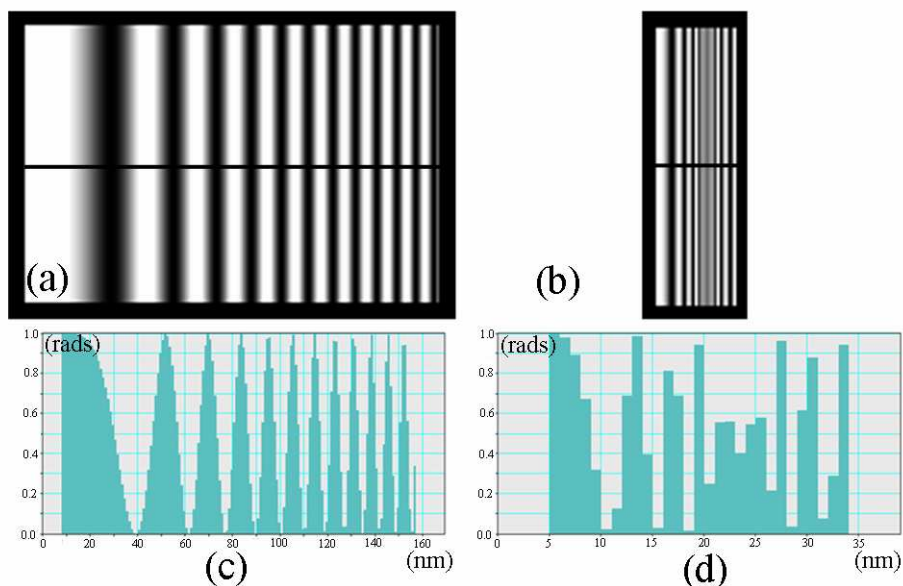


Fig.4.4 (a) A simulated line-spacing specimen with the size of 150 pixels $\times$ 100pixels; (b) the re-sampled specimen with the size of 30 pixels $\times$ 100 pixel; (c) and (d) are the profiles across the specimen in (a) and (b) along the line indicated, respectively.

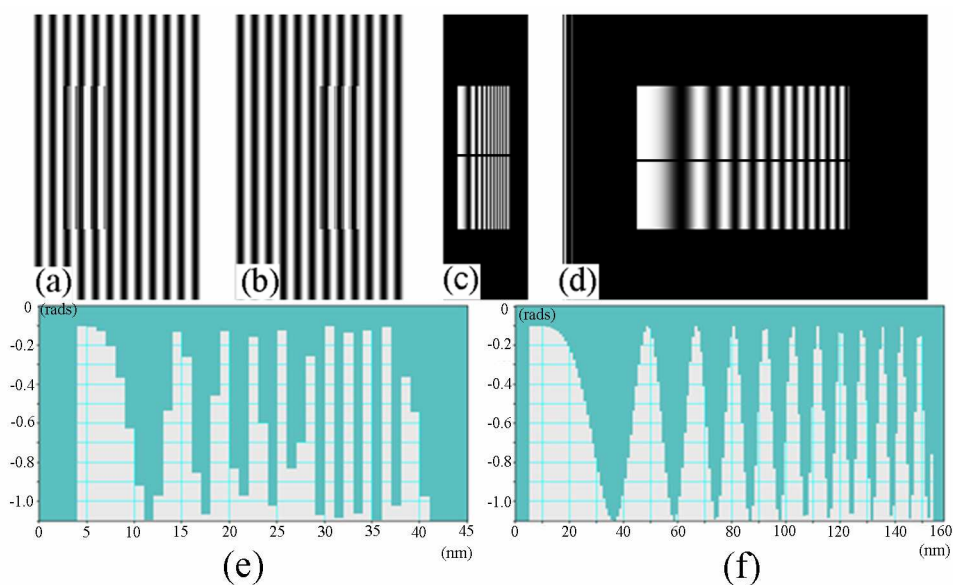


Fig.4.5 (a) and (b) are the holograms extracted from the simulated 3D data cube; (c) is the reconstructed phase image using one series of sliced interferograms; (d) is the interlaced phase image reconstructed by super-resolution technique, which is combined from several series of sliced interferograms; (e) and (f) are the profiles of the phase distribution across the specimen in (c) and (d) along the indicated lines, respectively.

#### 4.4 Experimental methods

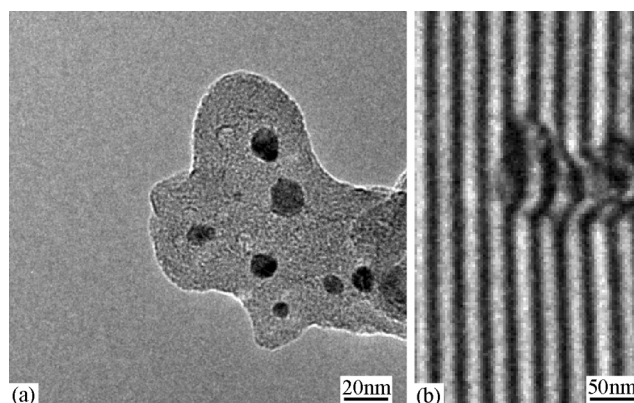


Fig.4.6 (a) TEM image of Co particles; (b) hologram of the Co particles extracted from the recorded 3D data cube.

The proposed technique was tested by observing Co particles experimentally. Figure 4.6(a) shows a bright-field TEM image of Co particles dispersed on a carbon film. The electron holography experiments were carried out at an accelerating voltage of 200 kV, using a JEOL JEM-ARM200F microscope equipped with a biprism and a stage-scanning system. A series of holograms as a 3D data cube with different specimen positions was recorded in a low magnification mode, in which the objective lens and the first intermediate lens were turned off. The specimen was moved stepwise along the  $x$ -axis by the stage-scanning system. The size of the recorded 3D data cube was 170 pixels $\times$ 280 pixels $\times$ 100 steps and the total acquisition time was about 1 min 50 s, including the data transfer time and 1-second exposure at each scan step. Figure 5(b) shows an extracted hologram from the recorded 3D data cube. In the given lens setting the CCD pixel size corresponded to 2.7 nm; the fringe spacing was 10.5 pixels, and  $\Delta x$  was calculated as  $\frac{\Delta a}{\Delta n} = \frac{4}{5}$  pixels = 2.16 nm. In this case, according to Fig. 4.3, the first step was slicing the 3D data cube at  $x_k$ , counted by 4 pixels to form a series of sliced interferograms, and reconstructed from them a low-resolution phase image. We then repeated this procedure at four successive  $x$

positions from  $x_k$  to  $(x_k + 3)$  and obtained four low resolution phase images. By interlacing these four low resolution phase images, a super resolution phase image can be obtained.

#### 4.5 Results and discussion

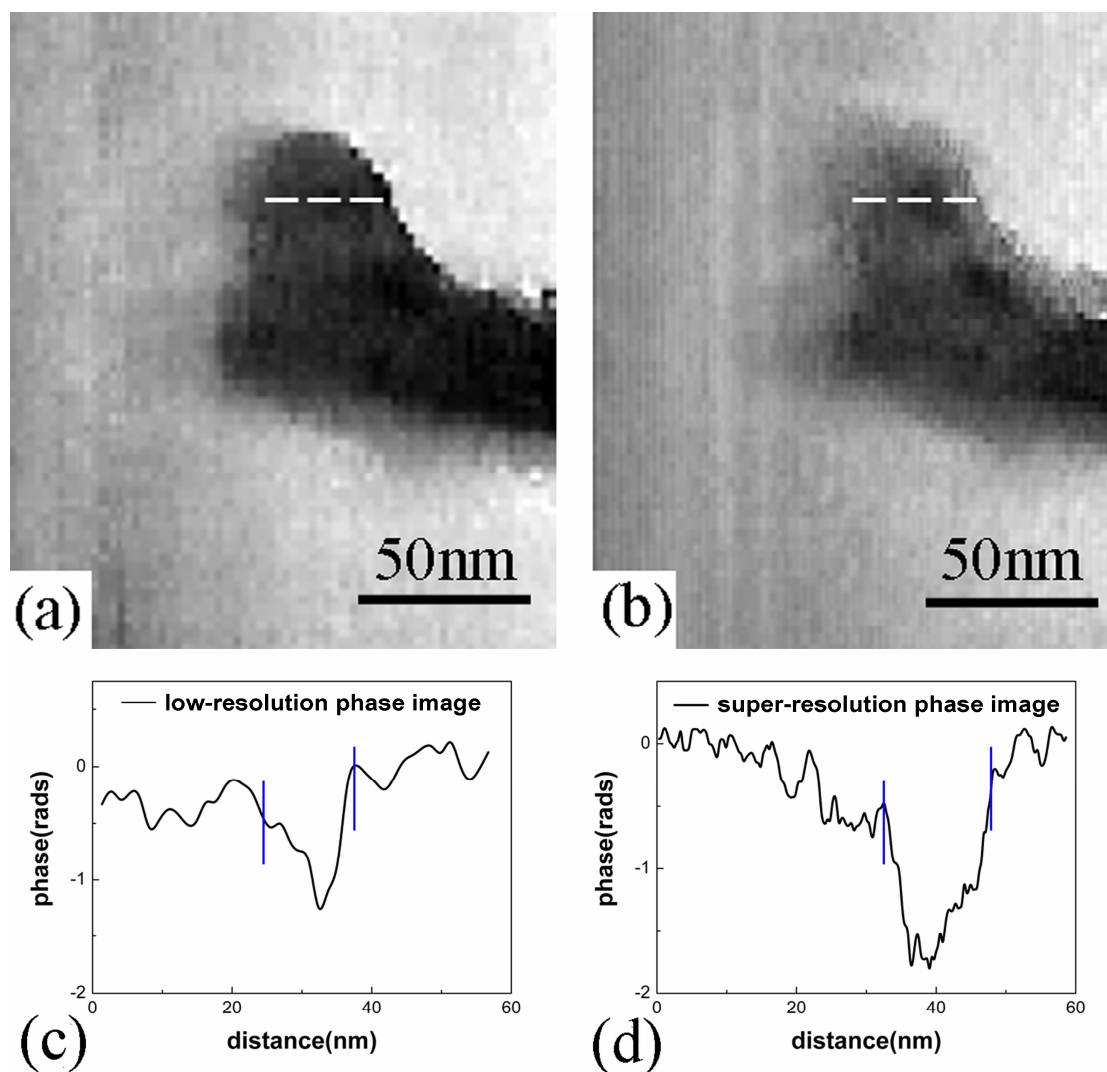


Fig.4.7 (a) Low-resolution phase image reconstructed from sliced interferogram; (b) super-resolution phase image obtained by interlacing the obtained low-resolution phase images; (c) and (d) are the phase profiles of the Co particle indicated by the dotted lines in (a) and (b), respectively.

One obtained low resolution phase image is shown in Fig. 4.7 (a). These four low-resolution phase images were then interlaced as outlined in Fig. 4.3 to obtain the

super-resolution phase image, which is shown in Fig. 4.7(b). The line profile in Fig. 4.7(d) shows the shape of the Co particle, which has a phase change of 1.2 radians. Its diameter is  $\sim 14.5$  nm, which is close to the value of 14.1 nm measured from the conventional TEM image of Fig. 4.6(a) along the same direction. However, in Fig. 4.7 (c), due to the lack of pixel numbers, the phase change is smaller than that estimated from the super-resolution image. The performance of the resolution improvement can be observed from the carbon edge, for example, in the low-resolution images (Fig. 4.7 (a)), the edges change abruptly due to the low pixel density. However, in the super-resolution phase image of Fig. 4.7 (b) the edge is smooth owing to the high pixel density.

This stage-scanning holography experiments were carried out in the low-magnification mode. In this case, the CCD pixel size divided by the magnification is much larger than the size calculated from the point spread function of the microscope used. Although the super-resolution phase reconstruction technique can overcome the CCD pixel-limited resolution due to the sub-pixel shift of the specimen, it may not overcome the resolution limit imposed by the point spread function. The super-resolution phase reconstruction technique is applicable not only in a low-magnification mode, but also in a high-magnification mode. However, additional experimental problems may appear at high magnifications, such as the insufficient precision of the piezo drive, as well as drifts of the biprism and specimen. The specimen drift may result in elongated shapes, whereas instabilities of the biprism will affect the image intensity. These effects will introduce phase errors in the reconstruction, but they can be reduced by improving the hardware.

#### 4.6 Fresnel diffraction effect

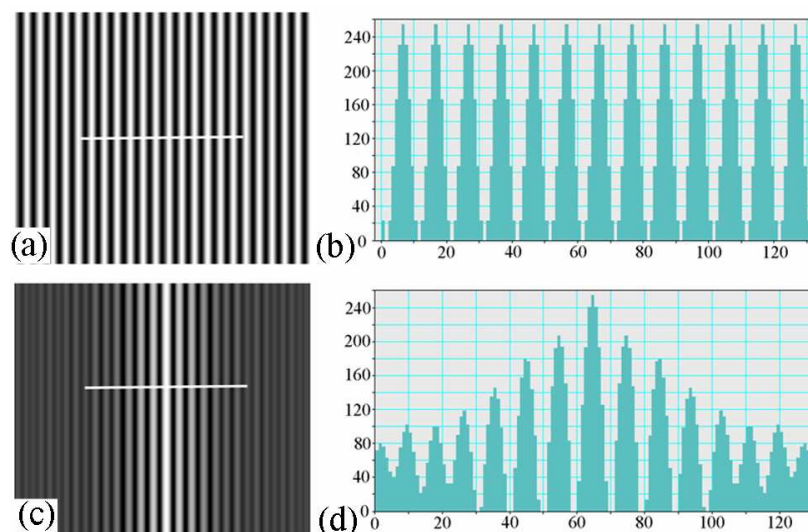


Fig. 4.8 Two simulated holograms without specimen: one is without Fresnel diffraction effect (a) and another is with Fresnel diffraction effect (c), respectively; (b) and (d) are the profiles along the lines indicated in (a) and (c).

One problem should be considered is the Fresnel diffraction effect. In the electron holography with the electron biprism, the Fresnel diffraction wave caused by the electron biprism overlaps with the interference fringes produced by the object and reference waves. This introduces a distortion in the amplitude of the electron wave, which results in non-uniform contrast of the interference fringes. When slicing the 3D data cube at different  $x$  positions, the intensity at each  $x$  position does not vary according to the cosine curve function, thus leading to the resultant phase errors in the reconstruction. Such phase error contributes to the periodic noise when interlacing the several phase images. In order to analysis the Fresnel diffraction effect in detail, two cases of different 3D data cube of holograms without specimen were simulated: one series of holograms without Fresnel diffraction effect (Fig. 4.8 (a)) and another series of holograms with Fresnel diffraction effect (Fig. 4.8 (c)). From the profiles shown in Fig. 4.8 (b) and (d), corresponding to the cases without and with Fresnel diffraction effect respectively, the intensity difference caused by Fresnel diffraction is clearly

observed. Slicing the 3D data cube at four successive  $x$  positions, results in four interferograms which are the cosine image of phase distribution. In the two cases, because there are no specimens, the amplitude  $\phi_0(-n\Delta x, y)$  can be replaced by 1 and the phase  $\eta(-n, y)$  is calculated as

$$\eta(-n, y) = \cos^{-1}\left(\frac{1}{2}\Pi(n, y) - 1\right).$$

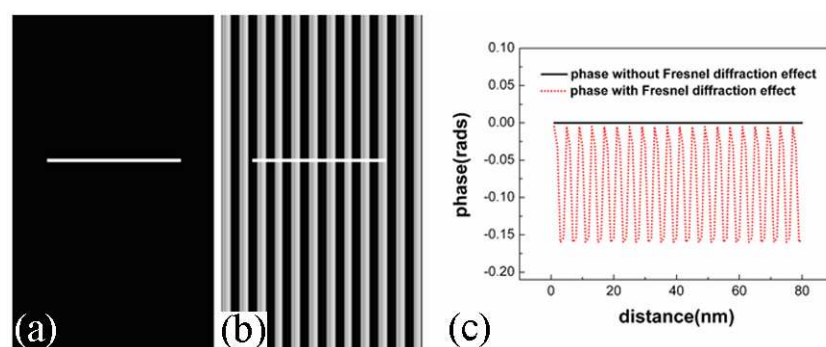


Fig.4.9 Reconstructed phase images from simulated holograms by super-resolution technique, (a) is the one without Fresnel diffraction effect and (b) is the one with Fresnel diffraction effect. (c) shows the profiles along the lines indicated in (a) and (b).

Four phase images can be calculated from the four sliced interferograms. After interlacing these four phase images, the super-resolution phase image can be obtained, as shown in the Figs. 4.9. The phase errors caused by the Fresnel diffraction effect can be clearly observed from the profiles shown in Fig. 4.9 (c). In this case, the phase error is about 0.16 rads. However, if the biprism voltage is increased, the Fresnel fringes will move to the edge of the overlapped area. Then if some fringes far from the region which contain Fresnel fringes are used for reconstruction, the accuracy of the phase measurement will be improved.

## **4.7 Conclusions**

A super-resolution phase reconstruction technique in electron holography is proposed in this chapter. Using a stage-scanning system, the specimen can be shifted with a fine step, and a 3D data cube can be recorded that contains holograms corresponding to different specimen positions. Slicing the data cube yields several low-resolution phase images with sub-pixel specimen shifts. A super-resolution phase image with a high pixel density can be obtained by interlacing these low-resolution phase images. The reconstructed super-resolution phase image provides high spatial resolution and accuracy through the observation of Co particles.

## Reference

- [1] S. C. Park, M. K. Park and M. G. Kang (2003) Super-resolution image reconstruction: a technical overview, *IEEE Singnal Processing Magazine*. **03**:1053-5888.
- [2] M. Elad and A. Feuer (1999) Super-resolution reconstruction of image sequences, *IEEE Trans. Pattern Anal. Machine Intelli.* **21**:817-834.
- [3] M. C. Chiang and T. E. Boult (2000) Efficient super-resolution via image wrapping, *Image Vision Computing* **18**: 761-771.
- [4] D. Rajan and S. Chaudhuri (2002) Generation of super-resolution images from blurred observations using an MRF model, *J. Math. Imaging Vision*. **16**: 5-15.
- [5] H. Stark and P. Oskoui (1989) High resolution image recovery from image-plane arrays, using convex projections, *J. Opt. Soc. Am. A*, **6**: 1715-1726.
- [6] B. C. Tom and A. K. katsaggelos (2001) Resolution enhancement of monochrome and color video using motion compensation, *IEEE Trans. Image Processing* **10**: 278-287.
- [7] T. Komatsu, K. Aizawa, T. Igarashi, and T. Saito (1993) Signal-processing based method for acquiring very high resolution image with multiple cameras and its theoretical analysis, *Proc. Inst. Elec. Eng.* **140(1)**:19-25.
- [8] S. Borman and R. L. Stevenson (1999) Super-resolution from image sequences- A review, *Proc. 1998 Midwest Symp. Circuits and Systems*, pp:374-378.
- [9] S. Chaudhuri, Ed., Super-Resolution Imaging. Norwell, MA: Kluwer, 2001.
- [10] H. Ur and D. Gross (1992) Improved resolution from sub-pixel shifted pictures, *CVGIP: Graphical Models and Image Processing* **54**: 181-186.
- [11] N. Nguyen and P. Milanar (2000) An efficient wavelet-based algorithm for image superresolution, *Proc. Int. Conf. Image Processing*, **2**:351-354.
- [12] R. Y. Tsai and T. S. Huang (1984) Multipleframe image restoration and registration, *Advances in Computer Vision and Image Processing*. Greenwich, CT: JAI Press Inc., pp:317-339.
- [13] M. S. Alam, J. G. Bognar, R. C. Hardie, and B. J. Yasuda (2000) Infrared image

registration and high-resolution reconstruction using multiple translationally shifted aliased video frames, *IEEE Trans. Instrum. Meas.* **49**:915-923.

[14] N. R. Shah and A. Zakhor (1999) Resolution enhancement of color video sequences, *IEEE Trans. Image Processing*, **8**:879-885.

[15] S. P. Kim, N. K. Bose, and H. M. Valenzuela (1990) Recursive reconstruction of high resolution image from noisy undersampled multiframe, *IEEE Trans. Acoust.* **38**: 1013-1027.

[16] N. K. Bose, H. C. Kim and H. M. Valenzuela (1993) Recursive implementation of total least squares algorithm for image reconstruction from noisy, undersampled multiframe, *Proc. IEEE Conf. Acoustics, Speech and Signal Processing, Minneapolis*, **5**:269-272.

[17] M. C. Hong, M. G. Kang and A. K. Katsaggelos (1997) An iterative weighted regularized algorithm for improving the resolution of video sequences, *Proc. Int. Conf. Image Processing*, **2**: 474-477.

[18] S. H. Rhee and M. G. Kang (1999) Discrete cosine transform based regularized high-resolution image reconstruction algorithm, *Opt. Eng.*, vol. **38**:1348-1356.

[19] M. G. Kang (1998) Generalized multichannel image deconvolution approach and its applications, *Opt. Eng.*, no.11, pp.2953-2964, 1998.

[20] M. C. Hong, M. G. kang and A. K. katsaggelos (1997) A regularized multichannel restoration approach for globally optimal high resolution video sequence, *SPIE VCIP*, **3024**:1306-1317.

[21] N. K. Bose, S. Lertrattanapanich and J. Koo (2001) Advances in superresolution using L-curves, *Proc. Int. Symp. Circuits and Systems*, **2**: 433-436.

[22] B. C. Tom and A. K. Katsaggelos (1995) Reconstruction of a high-resolution image by simultaneous registration, restoration, and interpolation of low-resolution images, *Proc. 1995 IEEE Int. Conf. Image Processing*, **2**: 539-542.

[23] D. Lei, K. Mitsuishi, K. Harada, M. Shimojo, D. Y. Ju and M. Takeguchi (2013) Direct acquisition of interferogram by stage scanning in electron interferometry, *Microscopy*, accepted.

[24] Q. Ru, J. Endo, T. Tanji and A. Tonomura (1991) Phase-shifting electron

holography by beam tilting, *Appl Phys Lett.* **59**: 2372(1991).

[25] Q. Ru, G. Lai, K. Aoyama, J. Endo and A. Tonomura (1994) Principle and application of phase-shifting electron holography. *Ultramicroscopy.* **55**: 209-220.

[26] M. Park, E. Lee, J. Park, M. G. Kang and J. Kim (2002) DCT-based high-resolution image reconstruction considering the inaccurate sub-pixel motion information, *SPIE Optical Engineering* **41**: 370-380. [27] B. Bascle, A. Blake and A.

Zisserman (1996) Motion deblurring and super-resolution from an image sequence, *Lecture Notes In Computer Science* **1065**: 571-582.

[28] N. Nguyen, P. Milanfar and G. H. Golub (2001) A computationally efficient image superresolution algorithm, *IEEE Transactions on Image processing* **10**: 573-583.

[29] S. Lertrattanapanich and N. K. Bose (2002) High resolution image formation from low resolution frames using delaunay triangulation, *IEEE Transaction on Image Processing.* **11**:1427-1441.

[30] N. Nguyen, P. Milanfar and G. H. Golub (2001) Efficient generalized cross-validation with applications to parametric image restoration and resolution enhancement, *IEEE Transactions on Image processing* **10**: 1299-1308.

[31] M. Takeguchi, M. Shimojo, M. Tanaka, R. Che, W. Zhang and K. Furuya (2006) Electron holographic study of the effect of contact resistance of connected nanowires on resistivity measurement, *Surf Interface Anal.* **38**: 1628-1631.

[32] M. Takeguchi, A. Hashimoto, M. Shimojo, K. Mitsuishi and K. Furuya (2008) Development of a stage-scanning system for high-resolution confocal STEM, *J Electron Microsc.* **57**:123-127.

[33] M. Takeguchi, K. Mitsuishi, D. Lei and M. Shimojo (2011) Development of sample-scanning electron holography, *Microsc Microanal.* **17**(Suppl 2):1230.

[34] K. Yamamoto, I. Kawajiri, T. Tanji, M. Hibino and T. Hirayama (2000) High precision phase-shifting electron holography, *J Electron Microsc.* **49**(1):31-39.

## Chapter 5 Conclusions

The successful development of the field-emission electron guns and the electron biprism make the use of electron holography practical. A number of schemes for electron holography have been proposed in recent materials research, in which off-axis electron holography is the widely used one. However, the spatial resolution of the reconstructed conventional electron holographic images, based on Fourier transformation, is essentially limited by the fringe spacing of the hologram. When a high spatial carrier frequency is introduced to improve the resolution, a decrease in the fringe contrast will reduce the signal-to-noise ratio.

In this thesis, a stage-scanning electron holography technique is proposed. In this technique the object wave can be determined independently of the fringe spacing, overcomes the problems caused by Fourier transformation. This technique is based on moving the specimen to create a series of holograms that have different specimen positions. Taking line intensities on the recorded holograms eliminates the carrier fringes in the holograms and yields the interferogram. Under phase object approximation, the object phase can be readily obtained from the interferogram without any reconstruction procedure.

This stage-scanning electron holography technique is further improved and extended for a non-phase object by recording a series of holograms as a 3D data cube at different specimen positions. Slicing the 3D data cube at different CCD pixels produces several interferograms. By applying the proposed reconstruction procedure to these interferograms the phase distribution can be reconstructed with high precision. This technique is expected to overcome the limitation of spatial resolution due to the fringe spacing. Experiments were carried out using the proposed stage-scanning holography and conventional off-axis electron holography, respectively. The results demonstrated the availability of this technique.

Experiments were performed for demonstration of the resolution enhancement by observing Co nanoparticles with the stage-scanning electron holography and compare the results with the conventional holography based on the Fourier transformation method. Higher spatial resolution was achieved compared with that of conventional electron holography based on the Fourier transformation method. The stage-scanning electron holography is thus useful in a low-magnification mode when fine fringes cannot be obtained due to the limited TEM magnification.

In the stage-scanning electron holography, a key parameter of the technique is the width of stage movement in a single scan step, in other words, scan step width. If the scanning step is a multiple of the CCD pixel size then the spatial resolution of the reconstructed phase image is determined by the CCD pixel size divided by magnification, or the microscope resolution. If the scan step size is an arbitrary, the holograms are recorded with sub-pixel specimen shifts. Because of the sub-pixel shift, these holograms contain different phase information, and their interlacing increases the pixel density in the final phase image, improving the spatial resolution beyond the CCD pixel size divided by the magnification. Therefore, we introduced super-resolution reconstruction technique into electron holography, outline the principle and applications of the super-resolution electron holography technique.

## **Acknowledgements**

I would like to express my gratitude to all those who helped me during the writing of this thesis. My deepest gratitude goes first and foremost to Professor Masayuki Shimojo, my supervisor, for his constant encouragement and guidance. Prof. Shimojo taught me the knowledge of electron microscopy and guided me to the world of nanomaterials. However, in the second year of my Ph.D, Prof. Shimojo moved to Shibaura Institute of Technology. Since then, we met and discussed with each other every week in National Institute for Materials Science (NIMS). I appreciate him for everything he did for me; he went to the trouble of driving to NIMS and provided me guidance and suggestions. Without his patient instruction and insightful criticism, the completion of this thesis would not have been possible.

I also would like to express my heartfelt gratitude to another supervisor of mine, Doctor Kazutaka Mitsuishi in National Institute for Materials Science, who taught me the principles and operations of transmission electron microscopy. He introduced me to the technique of electron holography and gave me the valued opportunity to study on one of the most advanced techniques about TEM. I could not forget that with his accompany, we worked until midnight for getting a perfect experimental data. When I felt lack of confidence in experiments, he always encouraged me to face the difficulties and to overcome them. I could not forget his patience and illuminating instruction to me when I wrote manuscripts. It is from that time that I realized what attitude I should have towards research and work.

In the second year of my doctor course, I changed to Professor Dongying Ju's laboratory due to the move of Prof. Shimojo to Shibaura Institute of Technology. I would like to acknowledge the guidance and support obtained from Prof. Ju, and the convenience in study and living he provided to me through these years.

I also thank Dr. Masaki Takeguchi in National Institute for Materials Science and Dr. Ken Harada in Advanced Measurement and Analysis center in Hitachi Ltd. for their useful discussions and help during my preparation of each paper. Dr. Takeguchi developed the stage-scanning system and provided it generously for me to perform the stage-scanning holography technique.

I am grateful to Dr. Iakoubovskii in National Institute for Materials Science for proofreading my manuscripts. He helped me to brush up the grammar and prose flow of my manuscripts. I thank Ms. Yoshiko Nakayama for the help in sample preparation. Other colleagues in the Transmission Electron Microscopy station in NIMS provided great help and convenience to me in the instrument operations, sample preparation etc., I would like to express my grateful to them together. Dr. Xiaobin Zhang is specially thanked for helpful discussion and the help provided during my life in Japan.

The life in Saitama Institute of Technology was enriched and happy. I want to give my thanks to Dr. Zhan Yu, Ming zhao, Ningning Zhou, Zhigang Qin and Gang Shi for the joy and laughter they brought into my life.

Finally, I would like to express my heartfelt thanks to my family. Their continuous supporting gave me great courage to overcome the difficulties during my life in Japan.

In Saitama Institute of Technology,

June, 2013

Dan Lei

## **Publication List**

### **Papers**

- 1 Lei D, Mitsuishi K, Harada K, Shimojo M, Ju D Y, and Takeguchi M (2013) Mapping of phase distribution in electron holography with a stage-scanning system. *Materials Science Forum*. 750:pp152-155.
- 2 Lei D, Mitsuishi K, Harada K, Shimojo M, Ju DY and Takeguchi M (2013) Direct acquisition of interferogram by stage scanning in electron interferometry, *Microscopy*, in press.
- 3 Lei D, Mitsuishi K, Harada K, Shimojo M, Ju DY and Takeguchi M (2013) Resolution improvement in stage-scanning electron holography: comparison with conventional electron holography, *ISRN Nanotechnology*, 2013, ID:368671.
- 4 Lei D, Mitsuishi K, Harada K, Shimojo M, Ju DY and Takeguchi M, Super-resolution phase reconstruction technique in electron holography with a stage-scanning system, *Japanese Journal of Applied Physics*, submitted.

### **Conference and proceedings**

- 1 Takeguchi M, Mitsuishi K, Lei D and Shimojo M (2011) Development of Sample-Scanning Electron holography, *Microsc. Microanal.* 17(Suppl 2): 1230-1231.
- 2 Takeguchi M, Mitsuishi K, Lei D and Shimojo M, Development of sample-scanning electron holography, The Japanese Society of Microscopy 2011, 16-18 May 2011, Fukuoka, Japan.

- 3 Lei D, Mitsuishi K, Harada K, Shimojo M, Ju D Y, and Takeguchi M, Observation of MgO crystals using a stage-scanning electron holography, The Japanese Society of Microscopy 2012,14-16 May, Tsukuba, Japan.
- 4 Mitsuishi K, Lei D, Harada K, Shimojo M, Ju D Y, and Takeguchi M, 試料走査電子線ホログラフィーにおける位相再生法の検討, The Japanese Society of Microscopy 2012,14-16 May, Tsukuba, Japan.
- 5 Lei D, Mitsuishi K, Harada K, Shimojo M, Ju D Y, and Takeguchi M, Direct phase acquisition in electron holography with a stage-scanning system, The Japan Institute of Metals and Materials, 2012, 17-19 Sep, Ehime, Japan.
- 6 Lei D, Ju D Y (2012) Effect of the heat treatment on the proportion of retained austenite in SKD-11, *20th Congress of International Federation for Heat Treatment and Surface Engineering*.
- 7 Lei D, Mitsuishi K, Harada K, Shimojo M, Ju D Y, and Takeguchi M, Super-resolution phase reconstruction technique in electron holography with a stage-scanning system, The Japanese Society of Microscopy 2013, 20-22 May, Osaka, Japan.
- 8 Lei D, Mitsuishi K, Harada K, Shimojo M, Ju D Y, and Takeguchi M, Super-resolution phase reconstruction technique in stage-scanning electron holography, The 4<sup>th</sup> international symposium on organic and inorganic electronic materials and related nanotechnologies, 2013, 17-20 June, Kanazawa, Japan.